Apatite texture, composition and O-Sr-Nd isotopic signatures record magmatic and fluid characteristics at the Black Mountain porphyry deposit, Philippines.

MingJian Cao[1,2]*, Noreen J. Evans[3], Pete Hollings[4], David R. Cooke[5,6], Brent I. A. McInnes[3], KeZhang Qin[1,2,7]

[1]Key Laboratory of Mineral Resources, Institute of Geology and Geophysics, Chinese Academy of Sciences, Beijing 100029, China

[2]Innovation Academy for Earth Science, Chinese Academy of Sciences, Beijing 100029, China

[3]School of Earth and Planetary Sciences/John de Laeter Centre, Curtin University, Perth, Western Australia 6945, Australia

[4]Geology Department, Lakehead University, 955 Oliver Road, Thunder Bay, Ontario P7B 5E1, Canada

[5]Transforming the Mining Value Chain, an Australia Research Council Industrial Transformation Research Hub, University of Tasmania, Hobart, Tasmania 7001, Australia

[6]Centre for Ore Deposit and Earth Sciences (CODES), University of Tasmania, Hobart, Tasmania 7001, Australia

[7]College of Earth and Planetary Sciences, University of Chinese Academy of Sciences, Beijing 100049, China

Corresponding author: email: caomingjian@mail.iggcas.ac.cn

Abstract

Apatite is a ubiquitous accessory mineral in a range of igneous rocks and its trace element and isotopic signatures can be modified during hydrothermal alteration. This study investigates the suitability of apatite as an indicator of the source, chemistry, and evolution of primary magma and hydrothermal fluids. *In situ* textural, elemental and O-Sr-Nd isotopic analyses were performed on apatite in thin sections of fresh and altered dioritic porphyries from the Black Mountain porphyry Cu deposit in the Philippines.

All studied apatite crystals have similar subhedral to euhedral elongate, triangular and hexagonal shapes, and show homogeneous textures under the microscope and in backscattered electron images. The apatite in fresh rocks displays yellow to yellow-green luminescence, whereas apatite from altered rocks has green to brown luminescence. Both show similar crystallization zoning under cathodoluminescence. The apatite in fresh rocks is characterized by high contents of Cl (1.31 ± 0.28 wt.%, 1σ) and Mn (1737 ±225 ppm), and low $X_{OH\text{-}apatite}$ (0.39 ± 0.03), Fe (675 ± 194 ppm), Mg (134± 44 ppm), Sr (275 ± 43) and Pb (0.5 ± 0.1 ppm). In contrast, apatite in altered rocks is characterized by lower Cl (0.58 ± 0.07 wt.%, 1σ) and Mn (1118 ±178 ppm), and higher $X_{OH\text{-}apatite}$ (0.55 ± 0.04), Fe (1304 ± 121 ppm), Mg (444± 68 ppm), Sr (603 ± 69) and Pb (1.7 ± 0.3 ppm). The content of rare earth elements (REE), Y, U, Th and Zr, and the Sr-Nd isotopic signatures are similar across all apatite grains ($^{87}Sr/^{86}Sr$ = 0.7032 to 0.7043, εNd(t) = +5.1 to +8.4). X‑ray maps and elemental and oxygen isotope across apatite in fresh and altered rocks are similar.

The distinct luminescence colours coupled with distinct mobile elemental compositions (Cl, OH, Mn, Mg, Fe, Sr, Pb), fingerprint the modification of primary magmatic apatite during interaction with hydrothermal fluids. The similar Sr isotopic ratios ($^{87}Sr/^{86}Sr$ = 0.7032 to 0.7043) but slightly different O isotopic signatures ($\delta^{18}O$ = +6.0 ± 0.3 ‰ versus +6.6 ± 0.3 ‰) in apatite from fresh and altered rocks is consistent with the same deep magma chamber source for both the magma and the hydrothermal fluids, and suggests significant fluid boiling in the hydrothermal fluids given that ^{18}O preferentially fractionates into the liquid relative to ^{16}O during fluid boiling. The similarity of immobile element (REE, Y, U, Th and Zr) contents in both types of apatite,

consistency of textures and Nd isotopic composition, and absence of dissolution-reprecipitation features all suggest that altered apatite retains magmatic characteristics and that fluid/rock interaction was minimal. The apatite in fresh rocks has a similar oxygen isotope composition as zircons from the same sample ($\delta^{18}O$ = +5.9 ± 0.3 ‰), indicating little to no oxygen isotope fractionation between zircon and apatite. In this case, apatite provides a good proxy for the oxygen isotopic composition of the magma. The Cl content of the primary magma, early high temperature fluid and later hydrothermal fluid can be estimated using the Cl contents of the magmatic and replacement apatite (0.33 to 0.48 wt.%, 5.2 to 7.3 wt.% and ~2.7 wt.%, respectively). This indicates a depletion of Cl from the early high temperature fluid to the hydrothermal fluid, consistent with fluid boiling.

This study demonstrates that cathodoluminescent texture, elemental composition (such as Cl, Mn, Mg, Fe, Sr, Pb), and Sr-O isotopic signatures in apatite can be altered during hydrothermal fluid alteration, whereas other components (REE, Y, U, Th and Zr) and the Nd isotopic composition are preserved. These features can be used to constrain the origin, chemistry, and evolution of primary magma and ore-forming hydrothermal fluids.

Keywords: Apatite; Cl contents; Trace elements; *In situ* O-Sr-Nd isotopes; Black Mountain porphyry Cu deposit

1. INTRODUCTION

Apatite [$Ca_5(PO_4)_3(F, Cl, OH)$] is a ubiquitous accessory mineral in most igneous rocks. The Ca-site typically accommodates large cations (e.g., Na^{+}, Mg^{2+}, Mn^{2+}, Fe^{2+}, Sr^{2+}, Ba^{2+}, Pb^{2+}, Y^{3+}, REE^{3+}, Th^{4+}, and U^{4+}), and the P-site commonly accommodates other highly charged cations (e.g., Si^{4+}, S^{6+}, As^{5+}, V^{5+}; Pan and Fleet, 2002). Development of techniques such as single collector laser ablation inductively coupled plasma mass spectrometry (LA-ICP-MS), laser ablation multi-collector inductively coupled plasma mass spectrometry (LA-MC-ICP-MS) and secondary ion mass spectrometry (SIMS) permits *in situ* analysis of the trace elements (rare earth elements (REE), Sr, U, Pb, Mn, halogens), and Sr-Nd and O isotopic signatures in apatite, that may record the crystallization history (Bizzarro et al., 2003; Fisher et al., 2011;Yang et al., 2014; Bruand et al., 2019). Apatite also preserves trace element and Nd isotopic characteristics from the time of crystallization (Sha and Chappell, 1999; Belousova et al. 2002a, 2002b; Chu et al., 2009; Fisher et al., 2011; O'Sullivan et al., 2020), and retains its volatile content (F, Cl, S; Peng et al., 1997; Pan and Fleet, 2002; McCubbin et al., 2015; Kim et al., 2017; Li and Hermann, 2017). The chemistry of apatite is widely used to constrain the features and genesis of igneous rocks (Sha and Chappell, 1999; Belousova et al., 2002b; Chu et al., 2009; O'Sullivan et al., 2020), and is used as a tracer of mineralization (e.g., Belousova et al., 2002a; Cao et al., 2012, 2013; Bouzari et al., 2016; Mao et al., 2016; Glorie et al., 2019).

Experimental studies of water/rock reactions have shown that the textures and chemistry of apatite can be significantly modified by moderate to high temperature (300 to 900ºC) fluids, such as H_2O-CO_2, acidic and alkalic fluids (Betkowski et al., 2016; Harlov and Förster, 2003; Harlov et al., 2005; Migdisov and Williams-Jones, 2014). The apatite in altered rocks from mineralized systems commonly shows replacement textures as well as significant geochemical (e.g., Mn, Mg, Fe, Sr, REE) and O-Sr-Nd isotope variations (Li and Zhou, 2015; Zhao et al., 2015; Bouzari et al., 2016; Zeng et al., 2016; Li et al., 2018; Cao et al., 2019b; Andersson et al., 2019; Palma et al., 2019). As apatite is a major phase (1–50 % modal) in iron oxide-apatite deposits and is usually large in size (crystals up to >1 cm), many studies have investigated *in situ* textures, elemental content Sr-Nd-O isotope ratios in apatite to constrain the nature of the fluids

that formed the iron oxide-apatite deposits (Harlov et al. 2002; Li and Zhou, 2015; Schoneveld et al. 2015; Zeng et al., 2016; Li et al., 2018; Cruz et al., 2019; Palma et al., 2019; Mercer et al., 2020). It is more difficult to conduct combined *in situ* textural, elemental and isotopic studies of apatite in igneous rocks from other magmatic/hydrothermal deposits due to its lower abundance (<1% modal) and smaller crystal size (commonly <200 μm). Bouzari et al. (2016) conducted limited *in situ* EPMA and LA-ICP-MS analyses of apatite in thin sections of fresh and altered rocks from porphyry copper deposits in British Columbia and showed variations of both texture and geochemistry (Cl, Mn, Fe, REE, Na). Most other studies have been conducted on apatite seperates which lack key contextual information (e.g., Cao et al., 2012; Xu et al., 2015; Mao et al., 2016; Chen et al., 2018).

The small Black Mountain porphyry Cu-Au deposit is located in the center of the Baguio district of Northern Luzon, Philippines (Waters et al., 2011) and comprises multiple phases of diorite porphyry emplacement (from 6.4 to 2.8 Ma) with different degrees of hydrothermal alteration. Our previous work investigated the textures, *in situ* chemistry and Sr isotope ratios of magmatic (plagioclase, amphibole, zircon, Fe-Ti oxides) and hydrothermal minerals (titanite, chlorite, epidote) in these rocks (Cao et al., 2018a,b, 2019a, 2020). Both fresh and altered rocks contain apatite crystals in thin section, providing an ideal natural laboratory for a comprehensive investigation of textural, elemental and isotopic variations of apatite during hydrothermal alteration at a porphyry Cu deposit. In this study, cathodoluminescence (CL) textures, major and trace element chemistry, Sr, Nd and O isotope ratios were determined in apatite located in thin section or in drilled chips from thin sections. Samples of fresh syn-mineralized rocks and altered pre- and syn-mineralized rocks were studied, and methods included electron probe microanalysis (EPMA), LA-ICP-MS and SIMS. In addition, O isotope ratios in zircons separated from the same samples were measured using SIMS. The aim of the study was to take a multi-method approach to an evaluation of the suitability of apatite to elucidate characteristics of the magmatic and hydrothermal fluids.

2. GEOLOGIC SETTING

The Baguio district of the Philippines is one of the world's premier mineral provinces, and contains potential resources of approximately 52 Moz of Au and 6.2 million tonnes of Cu (Malihan and Ruelo, 2009) in a variety of mineral deposit types including porphyry, epithermal, and skarn (Bellon and Yumul, 2000; Cooke and McPhail, 2001; Cooke et al., 2011; Waters et al., 2011). The geology of the Baguio district is described in detail by Waters et al. (2011), Hollings et al. (2011), and Cooke et al. (2011). The Ar/Ar ages of intrusive rocks at the Baguio district show that the porphyry-type mineralization of this district is related to Pliocene to Pleistocene arc magmatism (Waters et al., 2011) which had low- to medium-K calc-alkaline characteristics (Hollings et al., 2011). Hollings et al. (2013) identified multiple felsic intrusive phases within the Black Mountain system, including pre-mineralized diorite porphyry (~6.4 Ma), pre-mineralized Liw-Liw Creek andesite porphyry (~3.2 Ma), early mineralized diorite, syn-mineralized diorite porphyry (3.0 to 2.8 Ma), as well as mafic phases including pre-mineralized Liw-Liw Creek basaltic dikes (4.73 ± 0.17 Ma) and late-mineralized mafic rocks (~2.8 Ma; Fig. 1). All the felsic rocks have a low- to medium-K calc-alkaline affinity and depleted Sr-Nd isotope compositions (Hollings et al., 2013).

All the felsic rocks have porphyritic textures and are composed of plagioclase (30–50 vol %, 1.0–6.0 mm diam) and amphibole (5–15 vol %, 0.2–4.0 mm diam) in a groundmass of plagioclase, quartz, amphibole and biotite. Most euhedral plagioclase phenocrysts show well developed regular zoning or complex zonation with significant patchy zones which are coupled with significant geochemical (Ca, Na, Sr, Fe) and Sr isotope variations (Cao et al., 2018a,b, 2019a, 2020). Similarly, many euhedral amphibole phenocrysts have obvious core-rim zonation with distinct chemical compositions (e.g., Mg, Fe, Sr, Cr, Cu; Cao et al., 2018a,b). Oxides are predominantly magnetite over ilmenite, and titanite and zircon are rarely observed in the groundmass. The altered rocks are characterized by the replacement of plagioclase phenocrysts by epidote, replacement of fine-grained plagioclase in the groundmass by massive epidote, and widespread occurrence of epidote, chlorite, and calcite. Subhedral to anhedral replacement titanite rims commonly occur in the altered diorite porphyry. Sulfides

(pyrite, chalcopyrite) and ankerite occur in the altered diorite porphyry. All of the fresh and altered felsic rocks contain trace amounts of apatite in the groundmass.

3. ANALYTICAL METHODS

A Cambridge Image Technology Ltd. MK 4A model cold CL stage mounted on a petrographic microscope was used to study the internal texture of the apatite grains. The samples were irradiated in a vacuum chamber with an electron beam of approximately 15 kV and a current of 350 to 500 μA at the China University of Geosciences, Wuhan.

The major element compositions of apatite were measured at the Institute of Geology and Geophysics, Chinese Academy of Sciences (IGGCAS) in Beijing, using a JEOL-JXA8100 electron microprobe operated in wavelength dispersive spectrometer mode. The operating conditions were 15 kV accelerating voltage, 10 nA beam current and 5 μm probe beam with counting times of 20 s for Na, F, K, Mg, Si, Mn, P, Al, Cl, Sr, Ca and Ti, 10 s for S and Fe at their characteristic X-ray line. The following natural minerals and synthetic oxides were used for calibration: apatite (P), anhydrite (S), diopside (Ca, Mg and Si), jadeite (Al), hematite (Fe), synthetic MnO (Mn), albite (Na), orthoclase (K), celestite (Sr), tugtupite (Cl) and topaz (F). All data were corrected using the atomic number-absorption-fluorescence procedure. Considering the relatively large size of apatite (>100 μm) and in order to increase the data reliability, the mean values of two separate analyses around the same spot were used.

X-ray maps for Ca, P, Mn, F and Cl in the apatite crystal were performed in WDS mode using a CAMECA SX Five FE Electron Probe Microanalyzer at IGGCAS, with an accelerating voltage of 15 kV, a beam current of 50 nA, a 0.3 μm pixel size and dwell time of 5 ms. All analyses of apatite major element compositions are presented in Supplementary Table A.1. Considering challenges with measuring F due to the effects of anisotropic diffusion in apatite (Stormer et al., 1993), we do not put much emphasis on this data.

In situ LA-ICP-MS trace element analyses of apatite were carried out on thin sections using an Agilent 7700x quadruple inductively coupled plasma mass spectrometer (ICPMS) coupled to a Resonetics RESOlution S-155-LR 193nm excimer

laser ablation system at the GeoHistory Facility in the John de Laeter Centre, Curtin University, Perth, Australia. Following a 15 to 20 s period of background analysis, apatite were ablated with a 50 μm beam, for 45 s at a 7 Hz repetition rate, using a laser energy (measured at the sample surface) of 1.5 J/cm^2. The sample cell was flushed with ultra-high purity He (350 mL min^{-1}) and N_2 (3.8 mL min^{-1}). High-purity Ar was utilized as the carrier gas. NIST 610 was used as the primary standard with NIST 612 and BHVO-2G used as secondary standards and analysed in blocks between 10 unknown sample ablations. The internal reference isotope (^{43}Ca) utilized for apatite was determined from EPMA CaO values. Data reduction and concentration calculations were performed using the trace element data reduction scheme in Iolite 3.4 (Paton et al., 2011). The accuracy of trace element concentrations is typically better than 5% for most elements based on repeated analyses of secondary standards. LA-ICPMS analytical results for reference materials and apatite are listed in Supplementary Table A.2.

In order to compare the δ^{18}O values of apatite and zircon, both zircon and apatite from the same samples were analyzed using a Cameca IMS-1280 at the IGGCAS, Beijing. Based on petrographic features, 3 mm diameter round chips including apatite grains and surrounding minerals were drilled from thick thin sections using a Proxxon microdrill press TBH (220–240 V). These were embedded in an epoxy mount together with apatite standards (Durango and Qinghu). The separated zircon grains from the syn-mineralized diorite porphyry (BA08GS013 and BA08GS019) were embedded in an epoxy mount together with zircon standards (Penglai and Qinghu). *In situ* apatite and zircon O isotopes analytical procedures were similar to those reported by Li et al. (2010). The Cs^+ primary ion beam was accelerated at 10 kV, with an intensity of ca. 2 nA and a beam size of 10 mm. The ^{16}O and ^{18}O ion intensities were measured simultaneously in multi-collection mode using two off-axis Faraday cups. The relative 2σ errors given for the δ^{18}O analyses include both external and internal precision. The values of δ^{18}O were normalized to Vienna Standard Mean Ocean Water compositions, reported in standard per mil notation, and corrected for the instrumental mass fractionation factor (IMF). The IMF was obtained using Durango apatite as a reference and a δ^{18}O value of

9.4‰ (Trotter et al., 2008) for apatite, and using the Penglai zircon as a reference with a $\delta^{18}O$ value of 5.3‰ for zircon (Li et al., 2010). The Qinghu apatite and zircon were also analyzed as external standards in this study and yielded an average value of 5.2 ± 0.2 ‰ for apatite (n = 37, 1σ), and 5.5 ± 0.3 ‰ for zircon (n = 10, 1σ), in good agreement with the recommended $\delta^{18}O$ value of 5.4 ± 0.2 ‰ for zircon (Li et al., 2013) and demonstrating the very limited oxygen isotope fractionation between zircon and apatite (Bruand et al., 2019). Based on repeated measurement of the standard, external reproducibility of $^{16}O/^{18}O$ ratios was better than 0.3 ‰. Both apatite and zircon O isotopic analytical results for standards and minerals are listed in Supplementary Table A.3.

In situ Sr-isotope compositions of individual apatite grains were measured in two different labs using a Thermo-Finnigan Neptune MC-ICPMS equipped with a 193 nm excimer ArF laser ablation system at the IGGCAS in Beijing and using a Nu Plasma II MC-ICPMS equipped with a 193 nm excimer ArF laser ablation system (RESOlution S155) at the China University of Geosciences, Wuhan. In both labs, the analytical method utilized was similar and is summarized here. Following a 40 s period of background analysis, apatite were ablated with a 120 to160 μm beam, for 60 s at a 8 Hz repetition rate and an energy density of 10 J cm^{-2}. The Sr isotopic data were acquired by static multi-collection in low-resolution mode using nine Faraday collectors. Data reduction was completed offline and the potential isobaric interferences were accounted for in the following order: Kr, Yb^{2+}, Er^{2+} and Rb. Detailed description of the instrument and the laser ablation system has been given in Yang et al. (2014). At the IGGCAS, Sr isotopic ratios were obtained for repeated analyses of in-house standard Apatite 2 and Slyudyanka apatite standards, whereas at the China University of Geosciences, Sr isotopic ratios were obtained for repeated analyses of an in-house Coral standard. The standards yielded the following values: $^{87}Sr/^{86}Sr$ = 0.72656±8 (1σ) for Apatite 2 (n = 38), $^{87}Sr/^{86}Sr$ = 0.707682±63 (1σ) for Slyudyanka apatite (n = 21), 0.709154±52 (1σ) for Coral (n = 71). These are well within the accepted Sr isotopic composition (Apatite 2 $^{87}Sr/^{86}Sr$ = 0.72654±5 (2σ); Slyudyanka apatite $^{87}Sr/^{86}Sr$ = 0.707683±25 (2σ) based on more than ten analyses using TIMS and solution MC-ICPMS methods (Yang et al.,

2014); Coral $^{87}Sr/^{86}Sr$ = 0.70910±2 (2σ) based on TIMS analyses (Bizzarro et al., 2003)). In addition, the reliability of *in situ* Sr isotope analyses can be directly evaluated by monitoring the values of $^{84}Sr/^{86}Sr$ and $^{84}Sr/^{88}Sr$ which show similar values of ~0.0565 and ~0.00669 for all three standards, and values of ~0.0562 and ~0.00671 for apatite samples, similar to previous studies (Bizzarro et al., 2003; Yang et al., 2014). LA-MC-ICPMS Sr isotopic results for reference materials and apatite are listed in Supplementary Table A.4.

In situ Nd isotope compositions of individual apatite grains were measured over previous Sr isotope analysis positions using LA-MC-ICPMS at the IGGCAS, Beijing. A spot size of 120 μm was employed at an 8 Hz repetition rate and an energy density of 15 J cm^{-2}. Each spot analysis consisted of approximately 60 s of data acquisition. During the analyses, the isobaric interference of ^{144}Sm on the ^{144}Nd signal was evaluated and corrected according to McFarlane and McCulloch (2007). The detailed *in situ* Nd isotopic analytical technique has been described in Yang et al. (2014). Neodymium isotopic ratios obtained for repeated analyses of Madagascar (MAD) and Otter Lake apatite standards yielded the following values: $^{143}Nd/^{144}Nd$ = 0.511331±28 (2σ) and $^{147}Sm/^{144}Nd$ = 0.08145±23 (1σ) for MAD (n = 31), $^{143}Nd/^{144}Nd$ = 0.511933±25 (1σ) and $^{147}Sm/^{144}Nd$ = 0.08243±8 (1σ) for Otter Lake (n = 27). These are well within the accepted Nd isotopic composition for MAD $^{143}Nd/^{144}Nd$ = 0.511348±16 (2σ) and $^{147}Sm/^{144}Nd$ = 0.0818±5 (2σ), and for Otter Lake $^{143}Nd/^{144}Nd$ = 0.511940±9 (2σ) and $^{147}Sm/^{144}Nd$ = 0.0824±4 (2σ) based on several combined TIMS and solution MC-ICPMS analyses for each standard (Fisher et al., 2011; Yang et al., 2014). LA-MC-ICPMS Nd isotopic analytical results for reference materials and apatite are listed in Supplementary Table A.4.

4. RESULTS

4.1. Textural Characteristics

The textures of apatite grains in the fresh syn-mineralized diorite porphyry (013 and 030; Fig. 2A) and in altered rocks including pre-mineralized diorite porphyry (038, 026, 054; Fig. 2B), and syn-mineralized diorite porphyry (036 and 052; Fig. 2C), were

investigated using a microscope, backscattered electron (BSE) images and CL (Fig. 2). The analyzed apatite crystals in the fresh rocks are slightly bigger (long dimensions of 200–1650 μm) than the apatite grains in the altered rocks (long dimension of 90–350 μm). The apatite in fresh and altered rocks show similar crystal forms including elongate shapes with length/width ratios of 2 to 5 (Fig. 2D, E, F, P, Q), triangular shapes (Fig. 2I, N, R), and commonly hexagonal shapes (Fig. 2G, K, M). All apatite commonly shows homogeneous textures under the microscope and in backscattered electron images (Fig. 2D, G, I, K, N). The X‑ray maps of apatite in fresh rocks (013 and 030) show homogeneous Ca, P, F and Cl compositions (Fig. 3). However, under CL, apatite in fresh and altered rocks show distinct features.

Under CL, apatites from the unaltered diorite porphyry commonly display luminescence of yellow to yellow-green (Fig. 2E, F, H, J). The elongate apatite grains have homogeneous luminescence with weak zoning (Fig. 2E, F). The euhedral hexagonal and triangular apatite grains have homogeneous luminescence with relative clear growth zoning (Fig. 2G, J). Anhydrite inclusions are found in the euhedral hexagonal apatite (Fig. 2G). Calcite, characterized by red luminescence, was observed with apatite in fresh rocks.

In contrast, the apatites in propylitic altered diorite porphyry commonly display green to brown luminescence (Fig. 2L, M, O, Q, R). The euhedral hexagonal apatite grains have relatively homogeneous green luminescence with clear oscillatory zonations, and occur with calcite (Fig. 2L, M). The apatite crystals with brown luminescence in the altered rocks typically occur with calcite ± pyrite and have been partially replaced by green luminescent apatite along fractures or rims (Fig. 2O, P). Similarly, some elongate and triangular apatite crystals show homogeneous green luminescence and oscillatory zoning (Fig. 2Q, R).

4.2. Chemistry

Major, trace element, oxygen isotope and Sr-Nd isotope compositions of analyzed apatite are presented in Supplementary Data Tables A.1, A.2, A.3 and A.4, respectively, and are summarized in Table 1.

Apatite in fresh and altered rocks show distinct major elemental compositions (Fig. 4). For example, the apatite in fresh rocks (013 and 030) show relative higher contents of MnO (0.23 ± 0.04 wt.%, 1σ), Cl (1.31 ± 0.28 wt.%) and $X_{Cl\text{-}apatite}$ (18.5 ± 4.1 mol.%), but lower contents of FeO (0.10 ± 0.02 wt.%) and $X_{OH\text{-}apatite}$ (39.3 ± 2.6 mol.%), compared to the apatite in altered rocks (MnO = 0.15 ± 0.03 wt.%, Cl = 0.58 ± 0.07 wt.%, $X_{Cl\text{-}apatite}$ = 8.2 ± 1.0 mol.%, FeO = 0.17 ± 0.02 wt.%, $X_{OH\text{-}apatite}$ = 55.0 ± 3.8 mol.%; Fig. 4; Table A.1). The apatites have Na_2O (0.08 ± 0.04 wt.% versus 0.09 ± 0.04 wt.%), F (1.59 ± 0.19 wt.% versus 1.39 ± 0.15 wt.%) and SO_3 (0.17 ± 0.14 wt.% versus 0.18 ± 0.11 wt.%; Fig. 4; Table A.1) in fresh and altered rocks, respectively. The similarity of apatite minor element contents (such as Mn, Fe and Mg) determined by EPMA and LA-ICP-MS indicate the reliability of both methods and the homogeneity of the grains at the scale of analysis (Fig. A.1).

All 282 LA-ICP-MS analyses support the lower contents of Fe (675 ± 194 ppm, 1σ, n = 102), Mg (134 ± 44 ppm), Sr (275 ± 43 ppm), Pb (0.5 ± 0.1 ppm) and Ba (0.4 ± 0.1 ppm), but higher contents of Mn (1737 ± 225 ppm) in apatite from fresh rocks, compared to apatite from altered rocks (Fe = 1304 ± 121 ppm, Mg = 444 ± 68 ppm, Sr = 603 ± 69 ppm, Pb = 1.7 ± 0.3 ppm, Ba = 0.9 ± 0.2 ppm, Mn = 1118 ± 178 ppm, 1σ, n = 181; Fig. 5; Table A.2). In addition, apatite in fresh rocks has higher Sr/Y (7.2 ± 1.3) and Mn/Fe (2.7 ± 0.5), but lower Mg/Fe (0.20 ± 0.03), than apatite in altered rocks (Sr/Y = 4.1 ± 1.1, Mn/Fe = 0.9 ± 0.1, Mg/Fe = 0.34 ± 0.04; Fig. 5; Table A.2). All apatites contain negligible Rb (typically below the detection limit of 0.1 ppm), low Rb/Sr ratios, similar Y/Ho, Th/U and Sm/Nd and similar concentrations of Na, V, Ga, Zr, Y, REE, U and Th (Fig. 5; Table A.2). All apatites have chondrite-normalized rare earth element (REE) patterns with gradually decreasing REE from La to Lu, weak negative Eu anomalies ($Eu^* = Eu_N/[Sm_N*Gd_N]^{0.5}$: 0.84 ± 0.11 versus 0.75 ± 0.03) and strong light-REE (La-Gd) to heavy-REE (Tb-Lu) fractionation ($LREE_N/HREE_N$: 7.2 ± 1.3 versus 9.9 ±2.2; Fig. 6; Table A.2).

For fresh rocks (013-1, 013-2, 030-2), four subhedral to euhedral, large apatite crystals (013-1, 330 × 720 μm; 013-2, 330 × 1630μm; 030-2 grain 1, 380 × 840 μm; 030-2 grain 2, 250 × 660 μm) have a relatively homogeneous distribution of P_2O_5, F,

Cl, Fe, Mg, Mn, Sr, Y, La, Ce, Nd, Sm, Gd, Eu, Dy Ho, Er, Yb, Zr, Pb, Th and U across the analytical transect (Fig. 7). Two subhedral to euhedral apatite crystals in altered rocks (026-1, 420× 450 μm; 036-2, 210 × 320 μm; Fig. 8) also show homogeneous compositions (Fig. 7).

The apatite from fresh samples 013-1 and 030-2 has restricted $\delta^{18}O$ variations with values of +5.2 to +6.3 ‰ (mean = +5.9 ‰; 1σ = 0.3; n = 37) and +5.7 to +6.5 ‰ (mean = +6.2 ‰; 1σ = 0.2; n = 31), respectively (Fig. 8). The apatite in altered rocks (038-1, 054-2 and 036-1) show restricted but slighly higher $\delta^{18}O$ variations with values of +6.4 to +7.0 ‰ (mean = +6.7 ‰; 1σ = 0.2; n = 31), +6.0 to +6.6 ‰ (mean = +6.3 ‰; 1σ = 0.1; n = 35) and +6.3 to +7.4 ‰ (mean = +6.8 ‰; 1σ = 0.3; n = 31), respectively (Fig. 8).

The analyzed zircons from the syn-mineralized diorite porphyry (013 and 019) typically have oscillatory zoning, euhedral and prismatic forms with length/width ratios ranging from 1:1 to 3:1, and crystal lengths of ~100–300 μm (Fig. 8). Similar to the apatite in the fresh rocks (mean = +6.0 ‰; 1σ = 0.3; n = 68), the zircons have $\delta^{18}O$ values of +5.5 to +6.5 ‰ (mean = +5.9 ‰; 1σ = 0.2; n = 33; Fig. 8). In addition, $\delta^{18}O$ sub-perpendicular analytical transects were made across one large crystal (013-1) and six subhedral to euhedral apatite crystals in fresh rocks (013-1, 030-2), and also on two euhedral apatite crystals in altered rocks (038-1). All crystals show relatively homogeneous $\delta^{18}O$ values across the transects (Fig. 9).

The apatite in the fresh and altered rocks have restricted $^{87}Sr/^{86}Sr$ (0.7034 to 0.7042 and 0.7032 to 0.7043), $^{147}Sm/^{144}Nd$ (0.095 to 0.120 and 0.084 to 0.127), and restricted $^{143}Nd/^{144}Nd$ (0.51291 to 0.51304 and 0.51290 to 0.51306) (Fig. 10; Table A.4). Due to the very young crystallization age for these rocks (6.39 to 2.83 Ma; Hollings et al., 2013) and negligible Rb with very low Rb/Sr ratios, apatite $^{87}Sr/^{86}Sr$ ratios can be considered to be initial ratios. Apatites all have restricted εNd(t) values (+5.3 to +8.0 and +5.1 to +8.4), T_2DM values (170 to 390 Ma and 140 to 410) in fresh and altered rocks, respectively (Fig. 10; Table A.4).

5. DISCUSSION

391 **5.1. The cause of variations in apatite chemistry**

392 Three different models can explain the origin of distinct apatite characteristics in
393 fresh and altered rocks: (1) inheritance from primary magmas (e.g., Belousova et al.,
394 2002; Chu et al., 2009; Mao et al., 2016); (2) elemental diffusion (Ague and Baxter,
395 2007); and (3) fluid modification (Harlov and Förster, 2003; Harlov et al., 2005;
396 Migdisov and Williams-Jones, 2014; Li and Zhou, 2015; Zhao et al., 2015; Betkowski
397 et al., 2016; Bouzari et al., 2016; Migdisov et al., 2016; Zeng et al., 2016; Anenburg et
398 al., 2018; Li et al., 2018; Cao et al., 2019b; Palma et al., 2019).

399 Based on natural samples and experimental investigations, apatite chemistry has
400 been shown to closely reflect the composition of the host magma (e.g., Prowatke and
401 Klemme, 2006; Chu et al., 2009). Previous studies at Black Mountain have documented
402 the existence of two distinct magmas (andesitic and basaltic), which mixed in a deep
403 magma chamber (Hollings et al., 2013; Cao et al., 2018a,b, 2019a, 2020). For example,
404 phenocrysts of plagioclase, amphibole and clinopyroxene with distinct zonation are
405 consistent with the mixing of a mafic and intermediate magma to form the mineralized
406 intrusions. If the apatite crystals also record this process, they could be expected to
407 show variations across the analytical transects. However, neither apatite X-ray maps
408 nor transect compositions show significant variations in geochemistry or $\delta^{18}O$ (Figs. 3,
409 7, 9). In addition, the apatite compositions show restricted variations in chemistry with
410 no evidence for two distinct groups as seen in the other magmatic minerals (Figs. 4, 5,
411 8). Furthermore, all the porphyries show similar elemental compositions (Fig. 11),
412 except relatively enrichment of Pb in altered rocks which was probably due to
413 mobilization of Pb during hydrothermal alteration (You et al., 1996). Thus, the distinct
414 apatite chemistry in fresh and altered rocks was not inherited from the primary magmas.

415 Elemental diffusion across a crystal may cause variations in the mineral chemistry
416 dependant on the diffusion coefficient, crystal size and environment (Watson et al.,
417 1985; Cherniak, 2000, 2005). Previously published diffusion coefficients for apatite
418 suggest that F and Cl diffuse faster than Pb, Sr and Mn, which in turn, diffuse faster
419 than REE and U (e.g., Watson et al., 1985; Brenan, 1993; Cherniak, 2000, 2005). X-ray
420 mapping and compositional transects can be used to constrain elemental diffusion in

minerals (Ague and Baxter, 2007; Cao et al., 2014a). For example, Ague and Baxter (2007) demonstrated the existance of Sr diffusion in apatite based on Sr variations which were modeled to constrain the thermal history of related rocks. However, the homogeneous X‑ray maps (F and Cl; Fig. 3) and lack of variations in Mn, Sr, Pb and LREE in apatite from fresh and altered rocks at Black Mountain suggest that there was little or no elemental diffusion (Fig. 8). The minor variations of Y, HREE (Gd, Dy, Er, Yb), Zr and U in the apatites is likely the result of the crystallization of other minerals as suggested by the variations of Nb/Ta, Zr/Hf, Y/Ho in different minerals in our previous study (Cao et al., 2020). In addition, as the HREE and U are less mobile than F, Cl, Mn, Sr and LREE (Watson et al., 1985; Brenan, 1993; Cherniak, 2000, 2005), it is unlikely that elemental diffusion generated the minor variations in Y, HREE and U without creating variations in F, Cl, Mn, Sr and LREE. Thus, elemental diffusion did not cause the observed chemical variations in the apatite from fresh and altered rocks.

Studies of fluid-mineral interaction in experiments and on natural mineralized rocks have shown that the apatite structure, chemistry and O-Sr-Nd isotopic composition can be modified by moderate to high temperature (300° to 900°C) hydrothermal fluids including H_2O-CO_2, acidic and alkalic fluids (Harlov and Förster, 2003; Harlov et al., 2005; Migdisov and Williams-Jones, 2014; Li and Zhou, 2015; Zhao et al., 2015; Betkowski et al., 2016; Bouzari et al., 2016; Migdisov et al., 2016; Zeng et al., 2016; Anenburg et al., 2018; Li et al., 2018; Palma et al., 2019). Our previous studies at the Baogutu porphyry Cu deposit (China) have shown that low temperature (<300°C) fluids can modify the apatite structure, chemistry and Sr isotopic composition (Cao et al., 2019b). The altered rocks at Black Mountain are characterised by modifcation of plagioclase by epidote and of biotite by epidote and chlorite, as well as the widespread occurrence of calcite (Fig. 2). The apatite in altered rocks commonly occurs with calcite and sometimes with pyrite, epidote and ankerite (Fig. 2), and has higher contents of $X_{OH\text{-}apatite}$ (typically > 50 mol.%) relative to apatite in fresh rocks ($X_{OH\text{-}apatite}$ ~40 mol.%; Fig. 4). Yellow to yellow-green luminescence in apatite crystals from fresh rocks and green to brown luminescence in apatite from altered rocks, is consistent with that observed in fresh and altered apatite from porphyry copper deposits

in British Columbia (Bouzari et al., 2016). Therefore, both the mineral assemblage and the different apatite luminescence support hydrothermal replacement of apatite in altered rocks. In addition, the lower Mn and Cl contents in apatite from altered rocks relative to apatite from fresh rocks is also consistent with hydrothermal alteration (Bouzari et al., 2016).

The degree of replacement in apatite is strongly related to fluid composition, temperatures of the hydrothermal fluid and the fluid/apatite ratio (Palma et al., 2019). The replacement apatite commonly has obvious dissolution-reprecipitation textures (e.g., Harlov et al., 2002, 2005; Harlov and Förster, 2003; Li and Zhou, 2015; Bouzari et al., 2016; Broom-Fendley et al., 2016; Zeng et al., 2016; Li et al., 2018; Cao et al., 2019b; Palma et al., 2019). In addition, strong dissolution-reprecipitation of apatite is typically accompanied by depletion of REE and other elements and the occurrence of REE-rich minerals (such as monazite; Harlov et al., 2002, 2005; Harlov and Förster, 2003; Li and Zhou, 2015; Zeng et al., 2016; Li et al., 2018; Palma et al., 2019). Bouzari et al. (2016) indicated that the hydrothermal fluids related to relative low temperature phyllic alteration at porphyry Cu deposits can generate elemental variations (such as in Mn, Cl, REE, Y) and dissolution-reprecipitation textures in apatite. There are obvious elemental variations and different luminescences for apatite in fresh and altered rocks at Black Mountain, whereas the replaced apatite do not show dissolution-reprecipitation textures but rather partly retain their primary textures, including growth zonation, and comparable contents of Na, V, Ga, Zr, Y, REE, U and Th, and ratios of Y/Ho, Th/U and Sm/Nd (Fig. 5). Therefore, the fluids did not significantly modify either the texture or the chemistry of the magmatic apatite. We propose that a low fluid/apatite ratio is probably the major reason for the limited modification of the apatite in the Black Mountain intrusions, consistent with the low vein density and partial replacement of plagioclase by epidote in these rocks.

5.2. Apatite as a tracer of primary magma and hydrothermal fluids

5.2.1. Chlorine composition

Chlorine plays an important role in the evolution of magmatic systems and

associated ore deposits since it is one of the main ligands associated with metals and thus transports the metals from the magma to fluids in hydrothermal systems (e.g., Coulson et al., 2001; Williams-Jones and Heinrich, 2005). In magmatic systems, Cl is preferentially partitioned into apatite rather than the melt. The partitioning behavior of Cl between apatite and melt is non-Nernstian, and is a complex function of melt and apatite composition, Cl concentration and the pressure of the system (Webster and DeVivo, 2002; Mathez and Webster, 2005; Webster et al., 2009, 2017; Li and Hermann, 2017). Due to its non-Nernstian behavior, it is difficult to estimate the Cl content of melts using the published Nernst-style partition coefficients for Cl. The apatite in fresh rocks crystallized from the dioritic magma, and was not subsequently modified by hydrothermal fluids. As such, this apatite records the primary Cl content of the magma. To avoid the compositional interdependence of the components in the hydroxyl site of apatite, McCubbin et al. (2015) and Li and Hermann (2017) recommended using the Cl-OH exchange coefficients to estimate the contents of Cl in melts. Using this method, we determined the Cl melt content in equilibrium with apatite:

$C_{Cl\text{-}melt}$ (wt.%) = 10.79* ($X_{Cl\text{-}apatite}/X_{OH\text{-}apatite}$)*($1/Kd_{Cl\text{-}OH}^{ap\text{-}melt}$);

$Kd_{Cl\text{-}OH}^{ap\text{-}melt} = \exp[(25.81+17.33*(X_{Cl\text{-}apatite}-X_{OH\text{-}apatite})*1000/(8.314*T)]$;

where T is the equilibrium temperature between apatite and melt in °K.

Using the apatite saturation temperature ($T_{ap\ saturation}$; after Harrison and Watson, 1984) to represent the equilibrium temperature between apatite and the melt, $T_{ap\ saturation}$ is calculated to be ~860ºC for fresh samples 013 and 030 according to their whole rock (Hollings et al., 2013) and apatite compositions. We estimated the Cl melt concentrations to be 4756 ± 742 ppm (1σ) for the primary dioritic magma. Significant variations in the trace element composition of apatite (such as Cl, U, Y, Th/U, Sm/Nd; Figs. 4, 5) suggests that apatite crystallized over a wide range of temperatures. The effect of temperature on the calculated Cl concentration can be constrained using the mean zircon crystallization temperature (~710ºC; Cao et al., 2018a) as the minimum formation temperature of apatite according to the petrogenetic sequence of apatite > zircon for these rocks, and the higher saturation temperature of apatite than zircon (Cao et al., 2018a,b, 2019a). The Cl concentrations of the dioritic magma would decrease to

3313 ± 481 ppm (1σ) at ~710ºC. Thus, temperature can affect the Cl contents by up to 0.14 wt% in the diorite porphyry. The estimated 0.33 to 0.48 wt.% Cl is within the range of published Cl contents of melt inclusions from arc-related felsic systems which range from 0.05 to 0.7 wt.% (Webster et al., 2020), such as at the Augustine volcano, Alaska (0.14 to 1.35 wt.%; Roman et al., 2006), Dzarta-Khuduk, Mongolia (0.32 to 0.68 wt.%; Andreeva and Kovalenko, 2011), and Izu arc front, Pacific Ocean (0.21 to 0.73 wt.%; Straub and Layne, 2003). In addition, the values are also similar to other porphyry Cu deposit systems, such as the Dexing porphyry, China (0.15 to 0.43 wt.%; Bao et al., 2016), Deva porphyry, Romania (0.19 to 0.36 wt.%; Pintea, 2014), Cerro de Pasco mineralized granites, Peru (0.06 to 0.67 wt.%; Rottier et al., 2016), and Tyrone porphyry, Arizona (0.05 to 0.58 wt.%; Student and Bodnar, 2004).

Chlorine is preferentially partitioned into the fluid rather than the melt as high temperature fluids exsolve from the magma (Metrich and Rutherford, 1992; Webster and DeVivo, 2002; Williams-Jones and Heinrich, 2005). Large mineral systems and the associated hydrothermal alteration require the exsolution of large amounts of high temperature fluids from a deep magma chamber. Since the syn-mineralized diorite porphyry at Black Mountain was derived directly from the deep magma chamber, we use the Cl content of 0.33 to 0.48 wt.% to represent the Cl content in the deep magma chamber. Doherty et al. (2014) indicated that the partitioning behavior of Cl between fluid and melt depends on the molar (Al_2O_3/(Na_2O+K_2O+CaO)) ratio (A/CNK) of the whole rock, and can be expressed as:

$C_{Cl\text{-}fluid}$ (wt.%) = 14.8*$C_{Cl\text{-}melt}$ + 0.29, for A/CNK = 0.9 to 1.23.

The fresh rocks (013 and 030) have an A/CNK value of 0.9 (Hollings et al., 2013), so we can estimate the Cl content of the exsolved fluid to be 5.2 ± 0.7 wt.% and 7.3 ± 1.1 wt.% for melt Cl contents of 0.33 and 0.48 wt.%. The maximum salinity can be estimated to be 8.6 to 12.1 wt.% assuming all Cl combined with Na to form NaCl. Abundant Cl is required to form metal chloride complexes (e.g., Brugger et al., 2007; Mei et al., 2014) which transport metal from the deep magma chamber. The relatively low salinity of the exsolved high temperature fluid is consistent with typical estimates of preliminary single-phase supercritical fluid exsolved at depth (~2–13 wt.% NaCl

541 equivalent; Candela, 1989; Audétat and Pettke, 2003; Redmond et al., 2004; Audétat et
542 al., 2008).

543 On the other hand, Cl is also preferentially partitioned into the fluid phase rather
544 than into apatite (Webster et al., 2009), and the partitioning behavior of Cl between
545 apatite and the fluid is related to the molar ($Na_2O/(Na_2O + K_2O)$, N/NK) ratio of the
546 coexisting silicate melts (Doherty et al., 2014). The homogenous Cl contents of the
547 apatite crystals (Fig. 8J) suggests that apatite and the hydrothermal fluids were in
548 equilibrium. We can estimate the Cl content of hydrothermal fluid according to Doherty
549 et al. (2014):

550 $C_{Cl\text{-}fluid}$ (wt.%) = $(C_{Cl\text{-}apatite}\text{-}0.112)/(0.1897*(N/NK)^3/(A/CNK)^2)$

551 N/NK and A/CNK values for altered rocks are calculated to be 0.85 and 0.82,
552 respectively (Hollings et al., 2013). We estimate 2.7 ± 0.4 wt.% Cl in the equilibrated
553 hydrothermal fluids. This value is lower than the estimated Cl content of the preliminary
554 high temperature fluid exsolved at depth (5.2 to 7.3 wt.%), indicating significant fluid
555 boiling with a large proportion of Cl partitioning into the brine fluid and precipitation
556 of Cl as halite.

557

558 *5.2.2. The source*

559 Mineral fractional crystallization and high-temperature fluid exsolution will not
560 change the Sr-Nd isotope signatures in magmatic systems and their constituent minerals.
561 Thus, Sr-Nd isotope ratios in magmatic and hydrothermal apatite can be used to
562 constrain the source of the host rocks (Xu et al., 2015; Cao et al., 2017; Chen and Zhang,
563 2018). Apatite in the fresh rocks has a consistently high εNd(t) (+5.3 to +8.0) and low
564 $^{87}Sr/^{86}Sr$ (0.7034 to 0.7042) isotopic value (Table A.4; Fig. 10), similar to the value
565 determined for the whole rock and plagioclase (Figs. 10, 12), and consistent with a
566 mantle and/or juvenile lower crust source with minimal crustal contamination.

567 Only a few studies have investigated *in situ* apatite $\delta^{18}O$ values and their potential
568 as a proxy to trace the source of magma (Xu et al., 2015; Bruand et al., 2019; Sun et al.,
569 2019). Based on the results of SIMS oxygen isotopes for zircon, apatite and titanite,
570 Bruand et al. (2019) showed that apatite has a small oxygen isotope fractionation factor

571 relative to zircon (average $\Delta\delta^{18}O_{Zrn\text{-}Ap}$ = 0.4 ± 0.6 ‰, 1SD). However, the analysis of
572 Bruand et al. (2019) was conducted on seperated minerals in mounts, and representative
573 CL images of apatite crystals show very complex growth history with obvious core-rim
574 texture, in contrast to the relatively simple growth history for zircon as revealed by its
575 typically oscillatory zoning. Xu et al. (2015) reported similar core-rim textures for
576 seperated apatite in mounts and interpreted these to represent inherited cores and
577 crystallized rims. In this study, all the apatite was drilled from the thin sections and
578 analyzed for *in situ* $\delta^{18}O$ by SIMS. The texture of apatite in fresh rocks commonly
579 shows euhedral hexagonal shapes, homogeneous yellow to yellow-green luminescence
580 relative clear growth zoning (Fig. 2), indicating a simple continuous crystallization
581 history, consistent with their restricted chemical composition and uniform zircon
582 oscillatory zoning (Fig. 8). The apatite in fresh rocks shows similar $\delta^{18}O$ values (+6.0
583 ± 0.3‰, 1σ) to zircon (+5.9 ± 0.2‰, 1σ; Fig. 8, 12), indicating that there was little or
584 no oxygen isotope fractionation between zircon and apatite (average $\Delta\delta^{18}O_{Zrn\text{-}Ap}$ = 0.1).
585 Thus, apatite, like zircon, records the oxygen isotope composition of the magma. $\delta^{18}O$
586 values of 6.0 ± 0.3‰ for primary apatite are also compatible with a mantle and/or
587 juvenile lower crust source with minimal crustal contamination.

588 The Sr isotope ratios in hydrothermal or replacement apatite have also been used
589 to trace the source of hydrothermal fluids (Li and Zhou, 2015; Zhao et al., 2015; Zeng
590 et al., 2016; Li et al., 2018; Cao et al., 2019b; Palma et al., 2019). In this study, higher
591 Sr contents in replacement apatite in altered rocks relative to that of magmatic apatite
592 in fresh rocks (Fig. 5) indicates that the Sr contents and Sr isotope ratios in replacement
593 apatite record the features of hydrothermal fluids. Due to faster diffusion of oxygen in
594 apatite relative to other elements (e.g. Y, REE, U, Th; Cherniak, 2010), the Black
595 Mountain replacement apatite can record the $\delta^{18}O$ values of hydrothermal fluids, but
596 likely retain the REE compositions of primary magmatic apatite, consistent with
597 comparable Y, REE, U and Th contents in both fresh and altered apatite (Fig. 5). Thus,
598 the Sr and O isotope signatures in replacement apatite provide an opportunity to trace
599 the fluid source. For example, Zeng et al. (2016) indicated that the altered apatite from
600 the Taocun iron-oxide apatite deposit has higher $^{87}Sr/^{86}Sr$ ratios (0.7083 to 0.7097) but

601 lower $\delta^{18}O$ values (−3.0 to +3.4 ‰), compared to unaltered apatite ($^{87}Sr/^{86}Sr$ = 0.7077
602 to 0.7087; $\delta^{18}O$ = +5.3 to +7.5 ‰), and concluded that the interaction between apatite
603 and meteoric water was responsible for the Sr-O isotope signature of altered apatite. In
604 this study, the Sr-Nd isotopic characteristics in replacement apatite, whole rocks,
605 plagioclase phenocrysts, groundmass and hydrothermal epidote are similar (Fig. 12),
606 indicating that the fluids were mainly derived from the deep magma chamber. A deep
607 magma source for hydrothermal fluids is reported for most porphyry Cu deposits (e.g.,
608 Hedenquist and Lowenstern, 1994; Sillitoe, 2010; Richards, 2013).
609 The replacement apatite has a slightly higher average $\delta^{18}O$ value (6.6 ± 0.3 ‰, 1σ)
610 than the magmatic apatite (6.0 ± 0.3 ‰; Fig. 8, 13), which is in contrast to the similar
611 Sr isotope ratios in altered and magmatic apatite. An extra mechanism is required to
612 explain the decoupled Sr-O isotopes in the hydrothermal fluid. Assimilation of external
613 rocks or fluids typically generates coupled variations in Sr and O isotopes (e.g., Li et
614 al., 2016; Zeng et al., 2016). Water/rock interaction will decrease the $\delta^{18}O$ values of
615 fluids (e.g., Taylor, 1977; Cao et al., 2014b). Experimentally determined oxygen
616 isotopes fractionation factors at 130–600ºC have shown that ^{18}O preferentially
617 fractionates into the liquid relative to ^{16}O (Horita et al., 1995; Shmulovich et al., 1999).
618 However, slightly increased fluid $\delta^{18}O$ values during degassing and later hydrothermal
619 fluid boiling are widely recorded in porphyry copper systems (Hedenquist and
620 Lowenstern, 1994; Harris et al., 2005; Cao et al., 2014b). The replacement fluids at
621 Black Mountain have obviously lower Cl contents (2.7 ± 0.4 wt.%) than the calculated
622 preliminary high temperature fluid exsolved from the magma chamber (5.2 to 7.3 wt.%),
623 indicating the development of significant fluid boiling. During fluid boiling, the
624 residual fluids will have slightly increased $\delta^{18}O$ values but constant Sr isotopes.
625 Therefore, we propose that the decoupling replacement apatite Sr-O isotopes was
626 caused by fluid boiling and fluid/mineral (apatite) reactions.
627
628 *5.2.3. Conditions of formation of magmatic and replacement apatite*
629 The occurrence of magmatic anhydrite reflects sulfate saturation which requires
630 an oxidized (fO_2 > NNO + 1; Carroll and Rutherford, 1988; Jugo et al., 2005; Jugo,

631 2009) and sulfur enriched magma (Luhr, 1990; Chambefort et al., 2008). Magmatic
632 anhydrite has been observed in both arc-related volcanic rocks (Barth and Dorais, 2000;
633 Parat et al., 2002; Chambefort et al., 2008), and porphyry Cu deposits (Audétat et al.,
634 2004; Stern et al., 2007; Xiao et al., 2012; Cao et al., 2016, 2018a; Hutchinson and
635 Dilles, 2019). The anhydrite inclusions contained in magmatic apatite in this study
636 indicate an oxidized (fO_2 > NNO + 1) and sulfur-rich magma, consistent with our
637 previous conclusions (Cao et al., 2018a,b), based on amphibole Mg* (ΔNNO = 1.644
638 Mg*– 4.01; the definition of Mg* is given in Ridolfi et al., 2010), coexisting magnetite-
639 ilmenite (Lepage, 2003), and zircon Ce^{4+}/Ce^{3+}* (after Ballard et al., 2002). In addition,
640 the positive relationship between Na and S (atoms per formula unit, a.p.f.u.; Fig. 13A)
641 indicates the coupled substitution reaction $Na^{+} + S^{6+} = Ca^{2+} + P^{5+}$ occurred (Pan and
642 Fleet 2002), which also suggests oxidized conditions as the sulfur occurs as sulfate.
643 The composition of the hydrothermal fluid can be inferred from the chemistry of
644 the precipitating or replacement minerals and the geochemical behavior of certain
645 elements. Zeng et al. (2016) described significantly decreased Mg, Sr and Fe contents
646 in altered apatite relative to primary apatite, which is in contrast to the results obtained
647 in this study. The consistent and obviously high contents of Mg (444 ± 68 ppm, 1σ), Fe
648 (1304 ± 121 ppm), Sr (603 ± 69 ppm) and Pb (1.7 ± 0.3 ppm) in replacement apatite,
649 comparable to apatite from fresh rocks (Table A2; Fig. 5), likely reflects high Mg, Fe,
650 Sr and Pb concentrations in the replacement hydrothermal fluid, probably related to the
651 release of elements into hydrothermal fluids during alteration (e.g., Humphris and
652 Thompson, 1978; Mühe et al., 1997; Harlavan and Erel, 2002). This is consistent with
653 the occurrence of coeval Mg-, Fe- and Sr-rich hydrothermal minerals, such as epidote
654 (FeO = 12.5 ± 1.3 wt.%, Sr = 633 ± 300 ppm, 1σ; Cao et al., 2020), chlorite (FeO =
655 17.0 ± 5.1 wt.%, MgO = 20.7 ± 3.4 wt.%, 1σ; Cao et al., 2020), and ankerite (FeO =
656 32.1 ± 4.6 wt.%, 1σ; our unpublished data). Our previous studies have also indicated
657 obvious higher contents of Pb in hydrothermal titanite relative to Pb in magmatic
658 titanite at Black Mountain (Cao et al., 2020).
659 The lower Mn contents (1118 ± 178 ppm, 1σ) and Mn/Fe ratios (typically >1.5) in
660 apatite from fresh rocks relative to apatite from altered rocks (Mn = 1737 ± 225 ppm,

Mn/Fe typically <1.4) is consistent with the results of Bouzari et al. (2016). Figure 13B shows a negative relationship between Mn and Mg+Fe+Sr+Pb in replaced apatite, which indicates substitution of Mn by Mg+Fe+Sr+Pb derived from the fluid during replacement. In contrast, the obvious positive correlation between Mn and Mg+Fe+Sr+Pb in magmatic apatite indicates coupled substitution of these elements into apatite during crystallization.

From 6.4 to 2.8 Ma, primary magmatic apatite crystallized during the high temperature magmatic stage in dioritic rocks derived from the deep felsic magma chamber. At 2.8 Ma, high temperature single-phase supercritical fluids with low salinity exsolved from the deep felsic magma chamber, and underwent significant fluid boiling during evolution and water/rock reactions. The evolved fluids contain slightly higher $\delta^{18}O$ isotopes but similar Sr-Nd isotopes to the preliminary fluids, developed relatively high contents of Mg, Fe, Sr and Pb during alteration, and then replaced the magmatic apatite (Fig. 14). Due to the relatively small amount of fluids (low water/rock ratio), the magmatic apatite were replaced with some modification to textures (yellow to yellow-green luminescence →green to brown luminescence), chemistry (decreased Cl, Mn, and increased Fe, Mg, Sr, Pb contents) and isotopes (slightly increased $\delta^{18}O$ values), without significantly modifying the relatively immobile elements (Y, REE, U, Th, Zr) and the Nd isotope ratio of apatite (Fig. 14).

5.3. Implications for petrogenesis and mineral exploration

Due to the wide spectrum of elements incorporated into its lattice and distinct luminescence textures in various hydrothermal systems, apatite is being increasingly used as an indicator of source rock type (Sha and Chappell, 1999; Belousova et al. 2002a, 2002b; Cao et al., 2013; O'Sullivan et al., 2020), and in mineral exploration (e.g. Belousova et al., 2002a; Cao et al., 2013; Bouzari et al., 2016; Mao et al., 2016; Glorie et al., 2019). For example, after comparing the apatite chemistry among mafic and felsic I-type and S-type granites, Sha and Chappell (1999) indicated that apatite from mafic I-type granites are characterized by right-inclined REE distribution patterns with strong LREE enrichment, weak to moderate negative Eu anomalies and low $(Sm/Nd)_{CN}$ ratios,

characteristics seen in the apatite studied in this work (Fig. 15A). O'Sullivan et al. (2020) further divided mafic I-type granitoids and mafic igneous rocks from other type of rocks according to the Sr/Y and LREE (La-Nd) values. All the Black Mountain apatite in both fresh and altered rocks have compositions similar to apatite from mafic I-type granites and mafic igneous rocks. Thus, apatite chemistry, especially the contents of Sr, Y, REE, can be a good indicator for petrogenesis, even if the rocks underwent some degree of hydrothermal alteration.

In order to investigate the potential of apatite as a useful resistate indicator mineral in exploration, Belousova et al. (2002a) and Cao et al. (2012) compared the elemental variations in apatite from different styles of mineralization and suggested that trace elements in apatites (e.g., Sr, Mn, Y, REE) could be used in exploration. Mao et al. (2016) further proposed some discriminant projections to distinguish between various ore deposit types. However, the Black Mountain magmatic and replacement apatite plot as two distinct groups, neither of which lie in the porphyry Cu deposit field (Fig. 15), suggesting that apatite chemistry alone is not a very accurate indicator of mineralization style, especially for rocks that have experienced significant hydrothermal alteration. Bouzari et al. (2016) reported a correlation between apatite luminescence and apatite chemistry (particularly based on Mn/Fe, Na and REE concentrations), and suggested that apatite texture and chemistry can be used to indicate the types of hydrothermal alteration in porphyry copper deposits, which is consistent with many other studies (Zeng et al., 2016; Cao et al., 2019b; Palma et al., 2019). Thus, the combination of apatite texture, chemistry and isotopes can more accurately fingerprint the type of hydrothermal alteration and mineralization.

6. CONCLUSIONS

The apatite in fresh and altered rocks show homogeneous textures but distinct luminescence (yellow to yellow-brown, green to brown). Compared to the apatite in fresh rocks, the apatite in altered rocks has distinct compositions of Cl, Mn, Fe, Mg, Sr and Pb, and a slightly different $\delta^{18}O$ value, suggesting mobilisation during hydrothermal alteration. These features suggest that apatite texture, chemistry and

721 isotopes can be modified by hydrothermal fluids. The decoupling of Sr-O isotopes in
722 altered apatite suggests fluid boiling in the preliminary high temperature magmatic fluid.
723 Altered and magmatic apatite have comparable concentrations of REE, Y, U, Th and Zr,
724 and also Nd isotope signatures, indicating retention of some primary magmatic
725 characteristics during hydrothermal alteration.

726 Anhydrite inclusions in magmatic apatite and plagioclase indicate an oxidized
727 (fO_2 > NNO + 1) and sulfur-rich magma, consistent with a positive relationship between
728 Na and S in apatite. The obvious negative relationship between Mn and Mg+Fe+Sr+Pb
729 in replaced apatite indicates the substitution of Mn by Mg+Fe+Sr+Pb from fluid in
730 altered apatite during replacement.

731 This study shows that textural studies, coupled with elemental composition and
732 Sr-Nd-O isotopic composition of apatite, can be used to characterize the magma and
733 hydrothermal fluid features.

734

735 **ACKNOWLEDGEMENTS**

736 We thank Gabe Sweet and Mike Baker for sample collection supported by the
737 Australian Mineral Industry Research Association project P765 and Anglo American
738 (Philippines), as well as Anne Hammond and Kristi Tavener of Lakehead University
739 for sample preparation. We thank XinFu Zhao for assistance with apatite CL at China
740 University of Geosciences, Di Zhang for assistance with major element analysis at
741 IGGCAS, Brad McDonald for assistance with LA-ICP-MS analysis at Curtin
742 University, YueHeng Yang for assistance with Sr-Nd isotopic analyses at IGGCAS,
743 KuiDong Zhao for assistance with Sr analysis at China University of Geosciences
744 (Wuhan), XiaoXiao Ling and QiuLi Li for assistance with O isotopic analysis at
745 IGGCAS. This work was supported by National Key Research and Development Plan
746 (2017YFC0601306), National Natural Sciences Foundation of China (41672090), and
747 Youth Innovation Promotion Association CAS (2018086) to Mingjian Cao. The
748 Australian Resource Characterisation Facility is supported by the Science and Industry
749 Endowment Fund (SIEF RI13-01). This study was enabled by AuScope (auscope.org.au)
750 and the Australian Government via the National Collaborative Research Infrastructure

751 Strategy (NCRIS). Additional financial support was provided by a Natural Sciences and
752 Engineering Research Council Discovery Grant to Pete Hollings.
753

754 **REFERENCES**

755 Andreeva I. A. and Kovalenko V. I. (2011) Evolution of the trachydacite and pantellerite
756 magmas of the bimodal volcanic association of Dzarta-Khuduk, central Mongolia:
757 investigation of inclusions in minerals. *Petrol.* **19**, 348–369.

758 Audétat A. and Pettke T. (2003) The magmatic-hydrothermal evolution of two barren
759 granites: a melt and fluid inclusion study of the Rito del Medio and Canada
760 Pinabete plutons in northern New Mexico (USA). *Geochim. Cosmochim. Acta* **67**,
761 97–121.

762 Audétat A., Pettke T. and Dolejš D. (2004) Magmatic anhydrite and calcite in the ore-
763 forming quartz-monzodiorite magma at Santa Rita, New Mexico (USA): Genetic
764 constraints on porphyry Cu mineralization. *Lithos* **72**, 147–161.

765 Audétat A., Pettke T., Heinrich C. A. and Bodnar R. J. (2008) The composition of
766 magmatic hydrothermal fluids in barren and mineralized intrusions. *Econ. Geol.*
767 **103**, 877–908.

768 Bao B., Webster J. D., Zhang D., Goldoff B. and Zhang R. (2016) Compositions of
769 biotite, amphibole, apatite and silicate melt inclusions from the Tongchang mine,
770 Dexing porphyry deposit, SE China: implications for the behavior of halogens in
771 this mineralized porphyry system. *Ore Geol. Rev.* **79**, 443–462.

772 Barth A. P. and Dorais M. J. (2000) Magmatic anhydrite in granitic rocks: First
773 occurrence and potential petrologic consequences. *Am. Miner.* **85**, 430–435.

774 Bellon H. and Yumul G. P. (2000) Mio-Pliocene magmatism in the Baguio mining
775 district (Luzon, Philippines): Age clues to its geodynamic setting. *Earth Planet.*
776 *Sci. Lett.* **331**, 295–302.

777 Belousova E. A., Griffin W. L., O'Reilly S. Y., Fisher N. I. (2002a) Apatite as an
778 indicator mineral for mineral exploration: trace-element compositions and their
779 relationship to host rock type. *J Geochem. Explor.* **76**, 45–69.

780 Belousova E. A., Griffin W. L., O'Reilly S. Y. and Fisher N. I. (2002b) Igneous zircon:

781 trace element composition as an indicator of source rock type. *Contrib. Mineral.*
782 *Petrol.* **143**, 602–622.
783 Betkowski W. B., Harlov D. E. and Rakovan J. F. (2016) Hydrothermal mineral
784 replacement reactions for an apatite-monazite assemblage in alkali-rich fluids at
785 300–600°C and 100 Mpa. *Am. Miner.* **101**, 2620–2637.
786 Bizzarro M., Simonetti A., Stevenson R. K. and Kurszlaukis S. (2003). In situ $^{87}Sr/^{86}Sr$
787 investigation of igneous apatites and carbonates using laser-ablation MC-ICP-MS.
788 *Geochim. Cosmochim. Acta* **67**, 289–302.
789 Bouzari F., Hart C. J. R., Bissig T. and Barker S. (2016) Hydrothermal alteration
790 revealed by apatite luminescence and chemistry: A potential indicator mineral for
791 exploring covered porphyry copper deposits. *Econ. Geol.* **111**, 1397–1410.
792 Brenan J. M. (1993) Partitioning of fluorine and chlorine between apatite and aqueous
793 fluids at high pressure and temperature: implications for the F and Cl content of
794 highP-T fluids. *Earth Planet. Sci. Lett.* **117**, 251–263.
795 Bruand E., Storey C., Fowler M., Heilimo E. and EIMF (2019) Oxygen isotopes in
796 titanite and apatite, and their potential for crustal evolution research. *Geochim.*
797 *Cosmochim. Acta* **255**, 144–162.
798 Brugger J., Etschmann B., Liu W., Testemale D., Hazemann J. L., Emerich H., Beek W.
799 v. and Proux O. (2007) An XAS study of the structure and thermodynamics of Cu(I)
800 chloride complexes in brines up to high temperature (400°C, 600bar). *Geochim.*
801 *Cosmochim. Acta* **71**, 4920-4941.
802 Candela P. A. (1989) Magmatic ore-forming fluids: thermodynamic and mass transfer
803 calculations of metal concentrations. In Ore Deposition Associated with Magmas
804 (eds Whitney J. A. and Naldrett A. J.). *Reviews Econ. Geol.* **4**, 203–221.
805 Cao M. J., Li G. M., Qin K. Z., Seitmuratova E. Y. and Liu Y. S. (2012) Major and trace
806 element characteristics of apatites in granitoids from Central Kazakhstan:
807 implications for petrogenesis and mineralization. *Resour Geol.* **62**, 63–83.
808 Cao M. J., Zhou Q. F., Qin K. Z., Tang D. M. and Evans N. J. (2013) The tetrad effect
809 and geochemistry of apatite from the Altay Koktokay No. 3 pegmatite, Xinjiang,
810 China: implications for pegmatite petrogenesis. *Mineral. Petrol.* **107**, 985–1005.

811 Cao M. J., Qin K. Z., Li G. M., Yang Y. H., Evans N. J., Zhang R. and Jin L. Y. (2014a)
812 Magmatic process recorded in plagioclase at the Baogutu reduced porphyry Cu
813 deposit, western Junggar, NW-China. *J. Asian Earth Sci.* **82**, 136–150.
814 Cao M. J., Qin K. Z., Li G. M., Evans N. J. and Jin L.Y. (2014b) Abiogenic Fischer–
815 Tropsch synthesis of methane at the Baogutu reduced porphyry copper deposit,
816 western Junggar, NW-China. *Geochim. Cosmochim. Acta* **141**, 179–198.
817 Cao M. J., Li G. M., Qin K. Z., Evans N. J. and Seitmuratova E. Y. (2016) Assessing
818 the magmatic affinity and petrogenesis of granitoids at the giant Aktogai porphyry
819 Cu deposit, Central Kazakhstan. *Am. J. Sci.* **316**, 614–668.
820 Cao M. J., Qin K. Z., Li G. M., Evans N. J., Hollings P., Maisch M. and Kappler A.
821 (2017) Mineralogical evidence for crystallization conditions and petrogenesis of
822 ilmenite-series I-type granitoids at the Baogutu reduced porphyry Cu deposit
823 (Western Junggar, NW China): Mössbauer spectroscopy, EPM and LA-(MC)-
824 ICPMS analyses. *Ore Geol. Rev.* **86**, 382–403.
825 Cao M. J., Hollings P., Cooke D. R., Evans N. J., McInnes B. I. A., Qin K. Z., Li G. M.,
826 Sweet G. and Baker M. (2018a) Physicochemical processes in the magma chamber
827 under the Black Mountain porphyry Cu-Au deposit (Philippines): Insights from
828 mineral chemistry and implications for mineralization. *Econ. Geol.* **113**, 63–82.
829 Cao M. J., Evans N. J., Hollings P., Cooke D. R., McInnes B. I. A., Qin K. Z. and Li G.
830 M. (2018b) Phenocryst zonation in porphyry-related rocks of the Baguio District,
831 Philippines: Evidence for magmatic and metallogenic processes. *J. Petrol.* **59**,
832 825–848.
833 Cao M. J., Evans N. J., Reddy S. M., Fougerouse D., Hollings P., Saxey D. W., McInnes
834 B. I. A., Mcdonald B. J. and Qin K. Z. (2019a) Micro- and nano-scale textural and
835 compositional zonation in plagioclase at the Black Mountain porphyry Cu deposit:
836 implications for magmatic processes. *Am. Miner.* **104**, 391–402.
837 Cao M. J., Evans N. J., Qin K. Z., Danišík M., Li G. M. and McInnes B. I. A. (2019b)
838 Open apatite Sr isotopic system in low-temperature hydrous regimes. *J. Geophys.*
839 *Res.: Solid Earth* **124**, 11192–11203.
840 Cao M. J., Hollings P., Evans N. J., Cooke D. R., McInnes B. I. A., Zhao K. D., Qin K.

841 Z., Li D. F. and Sweet G. (2020) In situ elemental and Sr isotopic characteristics
842 of magmatic to hydrothermal minerals from the Black Mountain porphyry deposit,
843 Baguio District, Philippines. *Econ. Geol.*, In press, doi:10.5382/econgeo.4701.
844 Carroll M. and Rutherford M. J. (1988) Sulfur speciation in hydrous experimental
845 glasses of varying oxidation state—results from measured wavelength shifts of
846 sulfur X-rays. *Am. Miner.* **73**, 845–849.
847 Chambefort I., Dilles J. H. and Kent A. J. R. (2008) Anhydrite-bearing andesite and
848 dacite as a source for sulfur in magmatic-hydrothermal mineral deposits. *Geology*
849 **36**, 719–722.
850 Chen L. and Zhang Y. (2018) In situ major-, trace-elements and Sr-Nd isotopic
851 compositions of apatite from the Luming porphyry Mo deposit, NE China:
852 Constraints on the petrogenetic-metallogenic features. *Ore Geol. Rev.* **94**, 93–103.
853 Chen M. H., Bagas L., Liao X., Zhang Z. Q. and Li Q. L. (2019) Hydrothermal apatite
854 SIMS Th–Pb dating: Constraints on the timing of low-temperature hydrothermal
855 Au deposits in Nibao, SW China. *Lithos* **324–325**, 418–428.
856 Cherniak D. (2000) Rare earth element diffusion in apatite. *Geochim. Cosmochim. Acta*
857 **64**, 3871–3885.
858 Cherniak D. (2005) Uranium and manganese diffusion in apatite. *Chem. Geol.* **219**,
859 297–308.
860 Cherniak D. (2010) Diffusion in Accessory Minerals: Zircon, Titanite, Apatite,
861 Monazite and Xenotime. *Rev. Mineral. Geochem.* **72**, 827–869.
862 Chu M., Wang K., Griffin W., Chung S., O'Reilly S., Pearson N. and Iizuka Y. (2009)
863 Apatite Composition: Tracing Petrogenetic Processes in Transhimalayan
864 Granitoids. *J. Petrol.* **50**, 1829–1855.
865 Cooke D. R. and McPhail D. C. (2001) Epithermal Au-Ag-Te mineralization, Acupan,
866 Baguio district, Philippines: Numerical simulations of mineral deposition. *Econ.*
867 *Geol.* **96**, 109–131.
868 Cooke D. R., Deyell C. L., Waters P. J., Gonzales R. I. and Zaw K. (2011) Evidence for
869 magmatic-hydrothermal fluids and ore-forming processes in epithermal and
870 porphyry deposits of the Baguio district, Philippines. *Econ. Geol.* **106**, 1399–1424.

871 Coulson I. M., Dipple G. M. and Raudsepp M. (2001) Evolution of HF and HCl activity
872 in magmatic volatiles of gold-mineralized Emerald Lake Pluton, Yurkon Territory,
873 Canada. *Mineral. Deposita* **26**, 594–606.
874 Cruz N. L. L., Simon A. C., Wolf A. S., Reich M., Barra F. and Gagnon J. E. (2019) The
875 geochemistry of apatite from the Los Colorados iron oxide–apatite deposit, Chile:
876 implications for ore genesis. *Mineral. Deposita* **54**, 1143–1156.
877 Doherty A. L., Webster J. D., Goldoff B. A. and Piccoli P. M. (2014) Partitioning
878 behavior of chlorine and fluorine in felsicmelt–fluid(s)–apatite systems at 50 MPa
879 and 850–950 °C. *Chem. Geol.* **384**, 94–111.
880 Fisher C. M., McFarlane C. R. M., Hanchar J. M., Schmitz M. D., Sylvester P. J., Lam
881 R. and Longerich H. P. (2011). Sm–Nd isotope systematics by laser ablation-
882 multicollector-inductively coupled plasma mass spectrometry: Methods and
883 potential natural and synthetic reference materials. *Chem. Geol.* **284**, 1–20.
884 Glorie S., Jepson G., Konopelko D., Mirkamalov R. and Grave J. D. (2019)
885 Thermochronological and geochemical footprints of post-orogenic fluid alteration
886 recorded in apatite: Implications for mineralisation in the Uzbek Tian Shan.
887 *Gondwana Res.* **71**, 1-15.
888 Harlavan Y. and Erel Y. (2002) The release of Pb and REE from granitoids by the
889 dissolution of accessory phases. *Geochim. Cosmochim. Acta* **66**, 837–848.
890 Harlov D. E., Andersson U. B., Förster H. J., Nyström J. O., Dulski P. and Broman C.
891 (2002) Apatite-monazite relations in the Kiirunavaara magnetite-apatite ore,
892 northern Sweden. *Chem. Geol.* **191**, 47–72.
893 Harlov D. E. and Förster H. J. (2003) Fluid-induced nucleation of REE phosphate
894 minerals in apatite: nature and experiment. Part II. Fluorapatite. *Am. Miner.* **88**,
895 1209–1229.
896 Harlov D. E., Wirth R. and Förster H. J. (2005) An experimental study of
897 dissolutionreprecipitation in fluorapatite: fluid infiltration and the formation of
898 monazite. *Contrib. Mineral. Petrol.* **150**, 268–286.
899 Harris A. C., Golding S. D. and White N. C. (2005) Bajo de la Alumbrera copper–gold
900 deposit: stable isotope evidence for a porphyry-related hydrothermal system

dominated by magmatic aqueous fluids. *Econ. Geol.* **100**, 863–886.

Harrison T. M. and Watson E. B. (1984) The behavior of apatite during crustal anatexis: equilibrium and kinetic considerations. *Geochim. Cosmochim. Acta* **48**, 1467–1477.

Hedenquist J. W. and Lowenstern J. (1994) The role of magmas in the formation of hydrothermal ore deposits. *Nature* **370**, 519–527.

Hollings P., Cooke D. R., Waters P. J. and Cousens B. (2011) Igneous geochemistry of mineralized rocks of the Baguio district, Philippines: Implications for tectonic evolution and the genesis of porphyry-style mineralization. *Econ. Geol.* **106**, 1317–1333.

Hollings P., Sweet G., Baker M., Cooke D. R. and Friedman R. (2013) Tectonomagmatic controls on porphyry mineralization: Geochemical evidence from the Black Mountain porphyry system, Philippines. *Soc. Econ. Geol. Spec. Publ.* **17**, 301–335.

Horita J., Cole D. R. and Wesolowski D. J. (1995) The activity–composition relationship of oxygen and hydrogen isotopes in aqueous salt solutions: III. Vapor–liquid water equilibration of NaCl solutions to 350ºC. *Geochim. Cosmochim. Acta* **59**, 1139–1151.

Humphris S. E. and Thompson G. (1978) Trace element mobility during hydrothermal alteration of oceanic basalts. *Geochim. Cosmochim. Acta* **42**, 127–136.

Hutchinson M. C. and Dilles J. H. (2019) Evidence for magmatic anhydrite in porphyry copper intrusions. *Econ. Geol.* **114**, 143–152.

Jugo P. J., Luth R. W. and Richards J. P. (2005) Experimental data on the speciation of sulfur as a function of oxygen fugacity in basaltic melts. *Geochim. Cosmochim. Acta* **69**, 497–503.

Jugo P. J. (2009) Sulfur content at sulfi de saturation in oxidized magmas. *Geology* **37**, 415–418.

Kim Y., Koecke B., Fiege B., Simon A. and Becker U. (2017) An ab-initio study of the energetics and geometry of sulfide, sulfite and sulfate incorporation in apatite; the thermodinamic basis for using this system as an oxybarometer. *Am. Min.* **102**,

1646–1656.

Li G. M., Cao M. J., Qin K. Z., Evans N. J., Hollings P. and Seitmuratova E.Y. (2016) Geochronology, petrogenesis and tectonic settings of pre- and syn-ore granites from the W-Mo deposits (East Kounrad, Zhanet and Akshatau), Central Kazakhstan. *Lithos* **252-253**, 16–31.

Li H. J. and Hermann J. (2017) Chlorine and fluorine partitioning between apatite and sediment melt at 2.5 GPa, 800 °C. *Am. Miner.* **102**, 580–594.

Li X. C. and Zhou M. F. (2015) Multiple stages of hydrothermal REE remobilization recorded in fluorapatite in the Paleoproterozoic Yinachang Fe–Cu–(REE) deposit, Southwest China. *Geochim. Cosmochim. Acta* **166**, 53–73.

Li X. C., Zhou M. F., Yang Y. H., Zhao X. F. and Gao J. F. (2018) Disturbance of the Sm-Nd isotopic system by metasomatic alteration: A case study of fluorapatite from the Sin Quyen Cu-LREE-Au deposit, Vietnam. *Am. Miner.* **103**, 1487–1496.

Li X. H.; Long W. G., Li Q. L., Liu Y., Zheng Y. F., Yang Y. H., Chamberlain K. R., Wan D. F., Guo C. H., Wang X. C. and Tao H. (2010) Penglai Zircon Megacrysts: A Potential New Working Reference Material for Microbeam Determination of Hf-O Isotopes and U-Pb Age. *Geostand. Geoanal. Res.* **34**, 117–134.

Li X. H., Tang G. Q., Gong B., Yang Y. H., Hou K. J., Hu Z. C., Li Q. L., Liu Y. and Li X. X. (2013) Qinghu zircon: A working reference for microbeam analysis of U-Pb age and Hf and O isotopes. *Chin. Sci. Bull.* **58**, 4647–4654.

Luhr J. F. (1990) Experimental phase relations of water- and sulfur-saturated arc magmas and the 1982 eruptions of El Chichón volcano. *J. Petrol.* **31**, 1071–1114.

Malihan T. and Ruelo N. (2009) The Baguio mineral district: A giant multiepisodic clustered copper gold system: www.rwg-tag.bravehost.com/Conferences/ Surigao/Presentations/jun09-13h30-ruelo%20and%20malihan. pdf.

Mao M., Rukhlov A. S., Rowins S. M., Spence J. and Coogan L. A. (2016) Apatite Trace Element Compositions: A Robust New Tool for Mineral Exploration. *Econ. Geol.* **111**, 1187–1222.

Mathez E. A. and Webster J. D. (2005) Partitioning behavior of chlorine and fluorine in the system apatite–silicate melt–fluid. *Geochim. Cosmochim. Acta* **69**, 1275–1286.

McCubbin F. M., Kaaden K. E. V., Tartèse R., Boyce J. W., Mikhail S., Whitson E. S., Bell A. S., Anand M., Franchi I. A., Wang J. H. and Hauri E. H. (2015) Experimental investigation of F, Cl, and OH partitioning between apatite and Fe-rich basaltic melt at 1.0–1.2 GPa and 950–1000 °C. *Am. Miner.* **100**, 1790–1802.

McFarlane C. R. M. and McCulloch M. T. (2007) Coupling of in-situ Sm–Nd systematics and U–Pb dating of monazite and allanite with applications to crustal evolution studies. *Chem. Geol.* **245**, 45–60.

Mei Y. Liu W. H., Sherman D. M. and Brugger J. (2014) Metal complexation and ion hydration in low density hydrothermal fluids: Ab initio molecular dynamics simulation of Cu(I) and Au(I) in chloride solutions (25–1000°C, 1–5000bar). *Geochim. Cosmochim. Acta* **13**, 196-212.

Mercer C. N., Watts K. E. and Gross J. (2020) Apatite trace element geochemistry and cathodoluminescent textures—A comparison between regional magmatism and the Pea Ridge IOAREE and Boss IOCG deposits, southeastern Missouri iron metallogenic province, USA. *Ore Geol. Rev.* **116**, 103129.

Metrich N. and Rutherford M. J. (1992) Experimental study of chlorine behavior in hydrous silicic melts. *Geochim. Cosmochim. Acta* **56**, 607–616.

Migdisov A. A., Williams-Jones A. E. Brugger E., J. and Caporuscio F. A. (2016) Hydrothermal transport, deposition, and fractionation of the REE: Experimental data and thermodynamic calculations. *Chem. Geol.* **439**, 13–42.

Migdisov A. A. and Williams-Jones A. E. (2014) Hydrothermal transport and deposition of the rare earth elements by fluorine-bearing aqueous liquids. *Mineral. Deposita* **49**, 987–997.

Mühe R., Peucker-Ehrenbrink B., Devey C. W. and Garbe-Schönberg D. (1997) On the redistribution of Pb in the oceanic crust during hydrothermal alteration. *Chem. Geol.* **137**, 67–77.

Palma G., Barra F., Reich M., Valencia V., Simon A. C., Vervoort J., Leisen M. and Romero R. (2019) Halogens, trace element concentrations, and Sr-Nd isotopes in apatite from iron oxide-apatite (IOA) deposits in the Chilean iron belt: Evidence for magmatic and hydrothermal stages of mineralization. *Geochim. Cosmochim.*

991 *Acta* **246**, 515–540.
992 Pan Y. M. and Fleet M. E. (2002) Compositions of the apatite-group minerals:
993 Substitution mechanisms and controlling factors. *Rev. Mineral. Geochem.* **48**, 13–
994 49.
995 Parat F., Dungan M. A. and Streck M. J. (2002) Anhydrite, pyrrhotite, and sulfur-rich
996 apatite: Tracing the sulfur evolution of an Oligocene andesite (Eagle Mountain,
997 CO, USA). *Lithos* **64**, 63–75.
998 Paton C., Hellstrom J., Paul B., Woodhead J. and Hergt J. (2011) Iolite: Freeware for
999 the visualisation and processing of mass spectrometric data. *J. Anal. At. Spectrom.*
1000 **26**, 2508–2518.
1001 Peng G., Luhr J. F. and McGee J. J. (1997) Factors controlling sulfur concentrations in
1002 volcanic apatite. *Am. Min.* **82**, 1210–1224.
1003 Pintea I. (2014) The magmatic immiscibility between silicate-, HSL-, and Fe-S-O melts
1004 from the porphyry (Cu-Au-Mo) deposits in the Carpathians (Romania): a review.
1005 *Rom. J. Earth Sci.* **87**, 1–32.
1006 Prowatke S. and Klemme S. (2006) Trace element partitioning between apatite and
1007 silicate melts. *Geochim. Cosmochim. Acta* **70**, 4513–4527.
1008 Redmond P. B., Einaudi M. T., Inan E. E., Landtwing M. R. and Heinrich C. A. (2004)
1009 Copper deposition by fluid cooling in intrusion-centered systems: new insights
1010 from the Bingham porphyry ore deposit, Utah. *Geology* **32**, 217–220.
1011 Richards J. P. (2013) Giant ore deposits formed by optimal alignments and
1012 combinations of geological processes. *Nature Geosci.* **6**, 911–916.
1013 Roman D. C., Cashman K. V., Gardner C. A., Wallace P. J. and Donovan J. J. (2006)
1014 Storage and interaction of compositionally heterogeneous magmas from the 1986
1015 eruption of Augustine Volcano, Alaska. *Bull. Volcanol.* **68**, 240–254.
1016 Rottier B., Kouzmanov K., Bouvier A. S., Baumgartner L. P., Wälle M., Rezeau H.,
1017 BendezúR. and FontbotéL. (2016) Heterogeneous melt and hypersaline liquid
1018 inclusions in shallow porphyry type mineralization as markers of the
1019 magmatichydrothermal transition (Cerro de Pasco district, Peru). *Chem. Geol.* **447**,
1020 93–116.

1021 Sha L. K. and Chappell B. W. (1999) Apatite chemical composition, determined by
1022 electron microprobe and laser-ablation inductively coupled plasma mass
1023 spectrometry, as a probe into granite petrogenesis. *Geochim. Cosmochim. Acta* **63**,
1024 3861–3881.
1025 Shmulovich K. I., Landwehr D., Simon K. and Heinrich W. (1999) Stable isotope
1026 fractionation between liquid and vapour in water–salt systems up to 600ºC. *Chem.*
1027 *Geol.* **157**, 343–354.
1028 Sillitoe R. H. (2010) Porphyry copper systems. *Econ. Geol.* **105**, 3–41.
1029 Stern C.R., Funk J.A., Skewes M.A. and Arévalo A. (2007) Magmatic anhydrite in
1030 plutonic rocks at the El Teniente Cu-Mo deposit, Chile, and the role of sulfur- and
1031 copper-rich magmas in its formation. *Econ. Geol.* **102**, 1335–1344.
1032 Straub S. M. and Layne G. D. (2003) The systematics of chlorine, fluorine, and water
1033 in Izu arc front volcanic rocks: Implications for volatile recycling in subduction
1034 zones. *Geochim. Cosmochim. Acta* **67**, 4179–4203.
1035 Student J. J. and Bodnar R. J. (2004) Silicate melt inclusions in porphyry copper
1036 deposits: identification and homogenization behavior. *Can. Mineral.* **42**, 1583–
1037 1599.
1038 Sun S. J., Yang X. Y., Wang G. J., Sun W. D., Zhang H., Li C. Y. and Ding X. (2019) In
1039 situ elemental and Sr-O isotopic studies on apatite from the Xu-Huai intrusion at
1040 the southern margin of the North China Craton: Implications for petrogenesis and
1041 metallogeny. *Chem. Geol.* **510**, 200–214.
1042 Sun S. S. and McDonough W. F. (1989) Chemical and isotopic systematics of oceanic
1043 basalts: implications for mantle composition and processes. In Magmatism in the
1044 Ocean Basins (eds. Saunders A. D. and Norry M. J.). *Geol. Soc. Spec. Publ.* **42**,
1045 313–345.
1046 Taylor H. P. (1977) Water/rock interactions and the origin of H_2O in granitic batholiths:
1047 thirtieth William Smith lecture. *J. Geol. Soc.* **133**, 509–558.
1048 Taylor S. R. and McLennan S. M. (1985) *The Continental Crust: Its Composition and*
1049 *Evolution.* Blackwell Scientific Publications, Oxford, p. 312.
1050 Waters P. J., Cooke D. R., Gonzales R. I. and Phillips D. (2011) Porphyry and

epithermal deposits and $^{40}Ar/^{39}Ar$ geochronology of the Baguio district, Philippines. *Econ. Geol.* **106**, 1335–1363.

Watson E. B., Harrison T. M. and Ryerson F. J. (1985) Diffusion of Sm, Sr, and Pb in fluorapatite. *Geochim. Cosmochim. Acta* **49**, 1813–1823.

Webster J. D. and DeVivo B. (2002) Experimental and modeled solubilities of chlorine in aluminosilicate melts, consequences of magma evolution, and implications for exsolution of hydrous chloride melt at Mt. Somma-Vesuvius. *Am. Miner.* **87**, 1046–1061.

Webster J. D., Tappen C. M. and Mandeville C. W. (2009) Partitioning behavior of chlorine and fluorine in the system apatite–melt–fluid. II: Felsic silicate systems at 200MPa. *Geochim. Cosmochim. Acta* **73**, 559–581.

Webster J. D., Goldoff B. A., Flesch R. N., Nadeau P. A. and Silbert Z. W. (2017) Hydroxyl, Cl, and F partitioning between high-silica rhyolitic melts-apatite-fluid(s) at 50–200 MPa and 700–1000 °C. *Am. Miner.* **102**, 61–74.

Webster J. D., Iveson A. A., Rowe M. C. and Webster P. M. (2020) Chlorine and felsic magma evolution: Modeling the behavior of an under-appreciated volatile component. *Geochim. Cosmochim. Acta* **271**, 248–288.

Williams-Jones A. E. and Heinrich C. A. (2005) Vapor transport of metals and the formation of magmatic-hydrothermal ore deposits. *Econ. Geol.* **100th Anniversary**, 1287–1312.

Xiao B., Qin K. Z., Li G. M., Li J. X., Xia D., Chen L. and Zhao J. X. (2012) Highly oxidized magma and fluid evolution of Miocene Qulong giant porphyry Cu-Mo deposit, southern Tibet, China. *Resour. Geol.* **62**, 4–18.

Xu W. G., Fan H. R., Hu F. F., Santosh M., Yang K. F. and Lan T. G. (2015) In situ chemical and Sr–Nd–O isotopic compositions of apatite from the Tongshi intrusive complex in the southern part of the North China Craton: Implications for petrogenesis and metallogeny. *J. Asian Earth Sci.* **105**, 208–222.

Yang Y. H., Wu F. Y., Yang J. H., Chew D. M., Xie L. W., Chu Z. Y., Zhang Y. B. and Huang C. (2014) Sr and Nd isotopic compositions of apatite reference materials used in U–Th–Pb geochronology. *Chem. Geol.* **385**, 35–55.

You C. F., Castillo P. R., Gieskes J. M., Chan L. H. and Spivack A. J. (1996) Trace element behavior in hydrothermal experiments: Implications for fluid processes at shallow depths in subduction zones. *Earth Planet. Sci. Lett.* **140**, 41–52.

Zeng L. P., Zhao X. F., Li X. C., Hu H. and McFarlane C. (2016) In situ elemental and isotopic analysis of fluorapatite from the Taocun magnetite-apatite deposit, Eastern China: Constraints on fluid metasomatism. *Am. Miner.* **101**, 2468–2483.

Zhao X. F., Zhou M. F., Gao J. F., Li X. C. and Li J. W. (2015) In situ Sr isotope analysis of apatite by LA-MC-ICPMS: constraints on the evolution of ore fluids of the Yinachang Fe-Cu-REE deposit, Southwest China. *Mineral. Deposita* **50**, 871–884.

Figure Caption

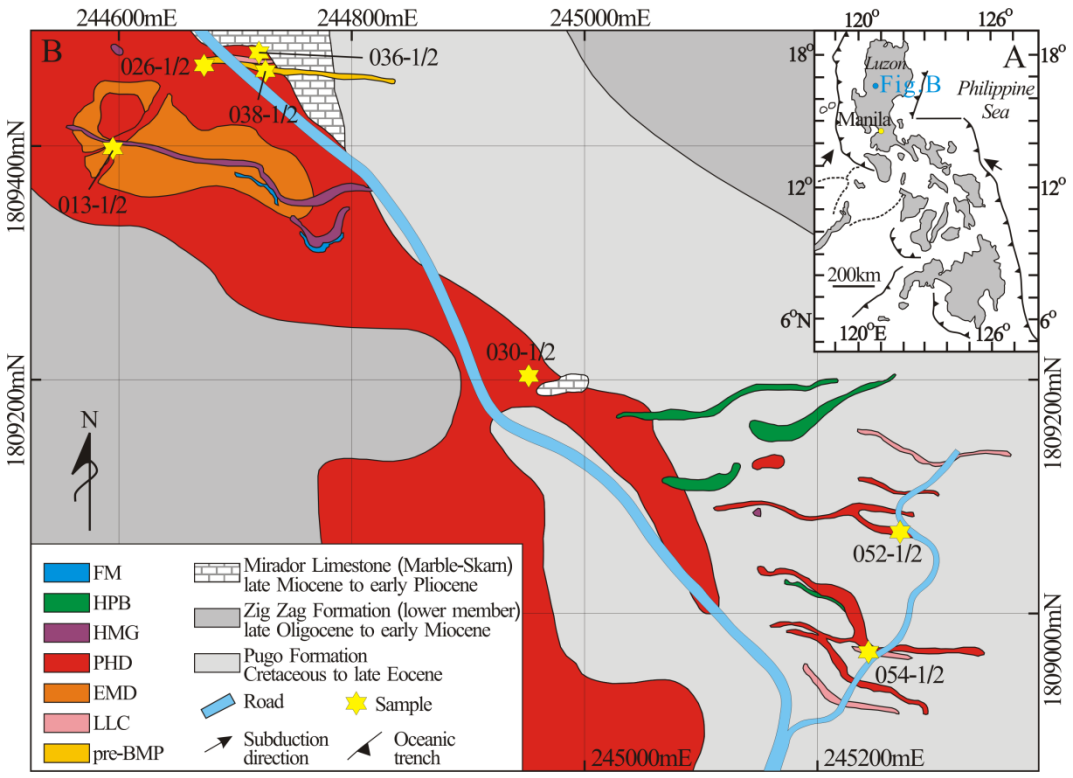

Fig. 1. (A) Map of the Philippines showing the location of the Black Mountain porphyry Cu-Au deposit. (B) Detailed geological map of the Black Mountain deposit after Hollings et al. (2013), showing the location of analyzed samples and surface distribution of the seven phases of intrusive rocks. From oldest to youngest: pre-mineralized plagioclase and hornblende diorite porphyry (pre-BMP), pre-mineralized Liw-Liw Creek basaltic to andesitic rocks (LLC), early mineralization diorite (EMD),

syn-mineralized plagioclase and hornblende diorite porphyry (PHD), late mineralized hornblende megacrystic gabbro (HMG), hornblende-phyric basaltic dike (HPB) and the fine-grained mafic dike (FM). Map coordinates in (B) are referenced to the Luzon Philippines datum, UTM zone 51.

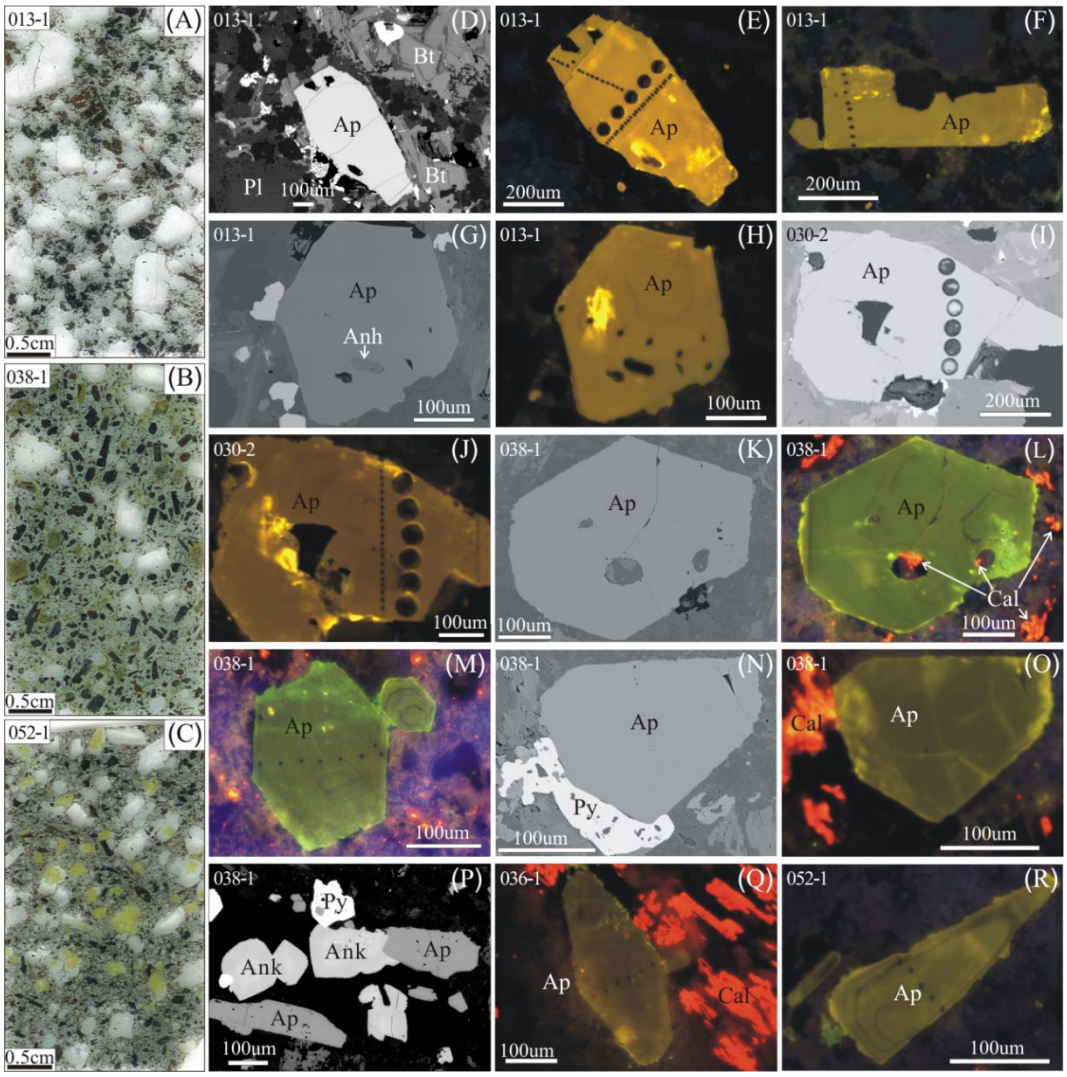

Fig. 2. Representative scans of whole thin sections showing absence of alteration for (A) syn-mineralized diorite porphyry sample (013-1), and obvious propylitic alteration for (B) pre-mineralized diorite porphyry sample (038-1) and (C) syn-mineralized diorite porphyry sample (052-1) from Cao et al. (2018a). BSE (D, G, I, K, N, P) and CL (E, F, H, J, L, M, O, Q, R) images of representative apatite grains from unaltered samples (013-1 and 030-2) and altered samples (038-1, 036-1 and 052-1). (D, E) Elongate apatite intergrown with biotite and plagioclase, showing yellow luminescence; (F) Elongate apatite showing yellow-green luminescence and growth zoning; (G, H)

Euhedral hexagonal apatite containing anhydrite inclusions and showing yellow luminescence with growth zoning in unaltered syn-mineralized diorite porphyry sample (013-1). (I, J) Apatite showing yellow luminescence and crystallization zoning; (K, L) Euhedral hexagonal apatite with clear fractures containing calcite inclusions and showing green luminescence and obvious growth zoning; (M) Euhedral hexagonal apatite showing green luminescence and very clear oscillatory growth zoning; (N, O) Triangular apatite occurring with pyrite and calcite and showing replacement texture of green luminescence overlapping brown luminescence around voids; (P) Elongate apatite containing voids and occurring with pyrite and ankerite in altered pre-mineralized diorite porphyry sample (038-1). (Q) Elongate apatite showing brown luminescence and occurring with calcite in altered syn-mineralized diorite porphyry sample (036-1). (R) Triangular apatite showing green luminescence and growth zoning in altered syn-mineralized diorite porphyry sample (052-1). Abbreviations: Anh = anhydrite; Ap = apatite; Ank = ankerite; Bt = biotite; Cal = calcite; Pl = plagioclase; Py = pyrite. The bright yellow area in CL images E, F, H, J was caused by uneven exposure.

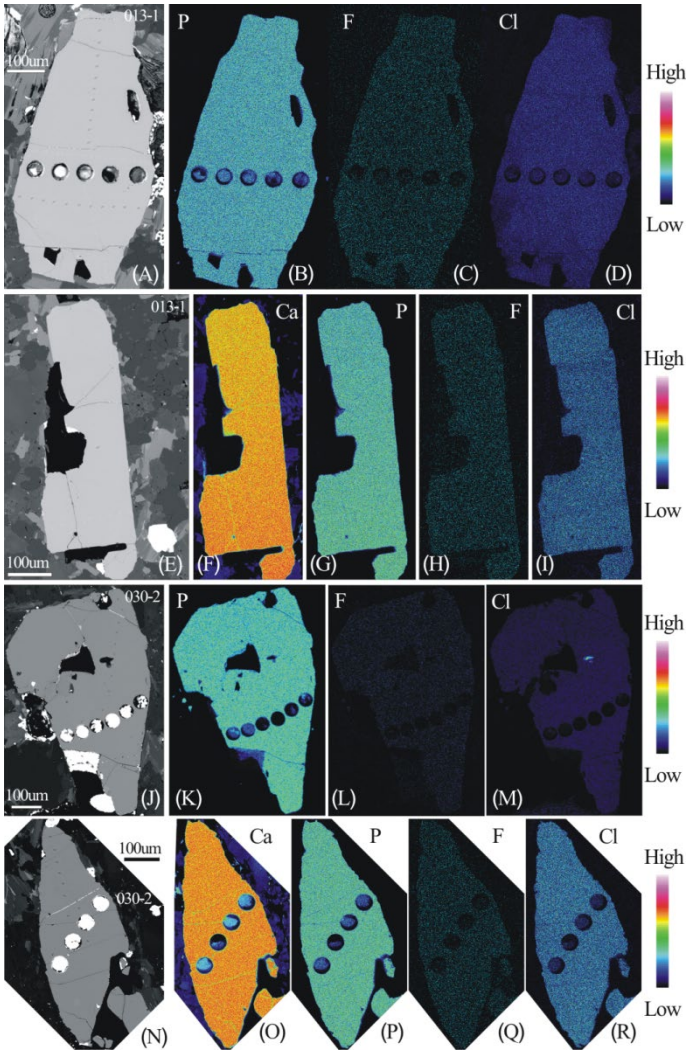

Fig. 3. Backscattered electron images (A, E, J, N) and X‑ray maps of P (B, G, K, P), Ca (F, O), F (C, H, L, Q) and Cl (D, I, M, R) showing the homogeneous Ca, P, F and Cl compositions for apatite samples from fresh rocks (013-1, 030-2) from the Black Mountain porphyry Cu deposit.

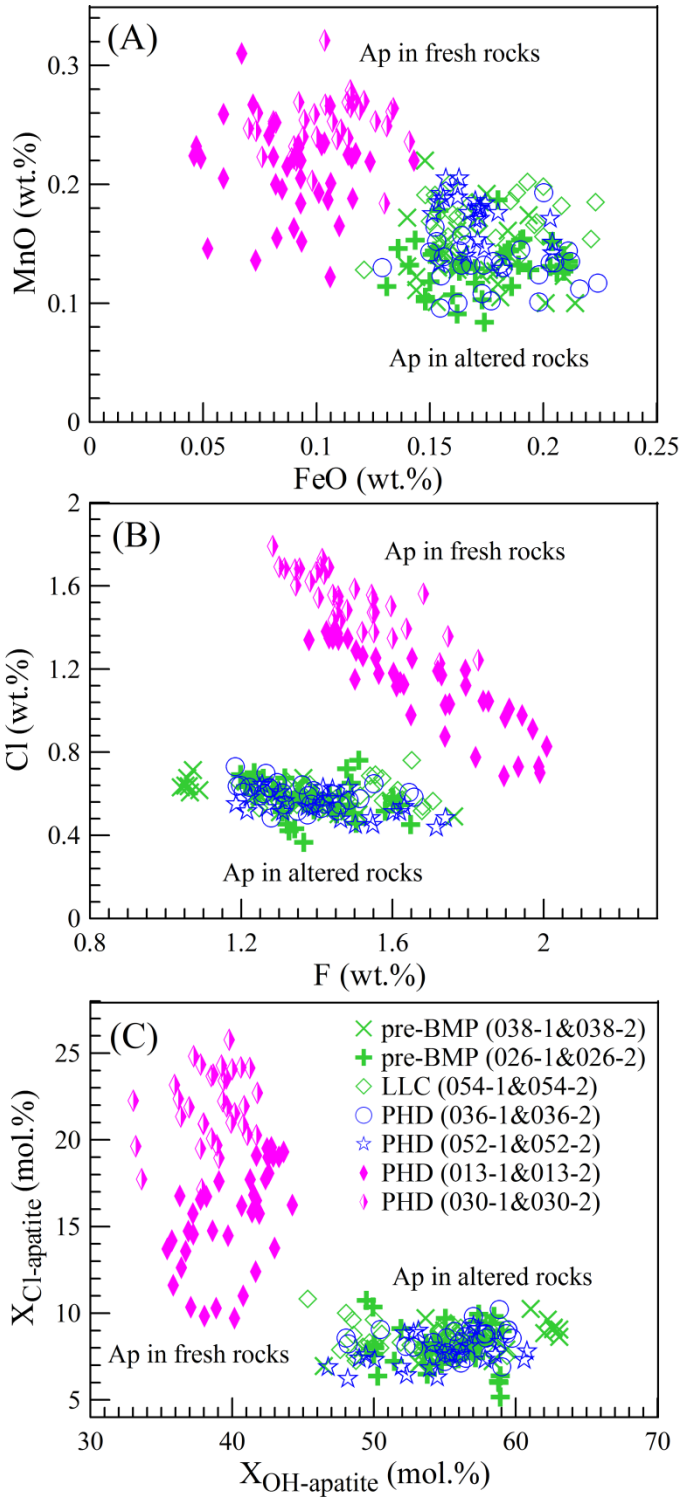

Fig. 4. Plots of (A) MnO versus FeO (wt.%), (B) Cl versus F (wt.%), and (C) $X_{Cl\text{-}apatite}$ versus $X_{OH\text{-}apatite}$ (mol.%) showing different elemental compositions for apatite from fresh and altered rocks at the Black Mountain porphyry Cu deposit.

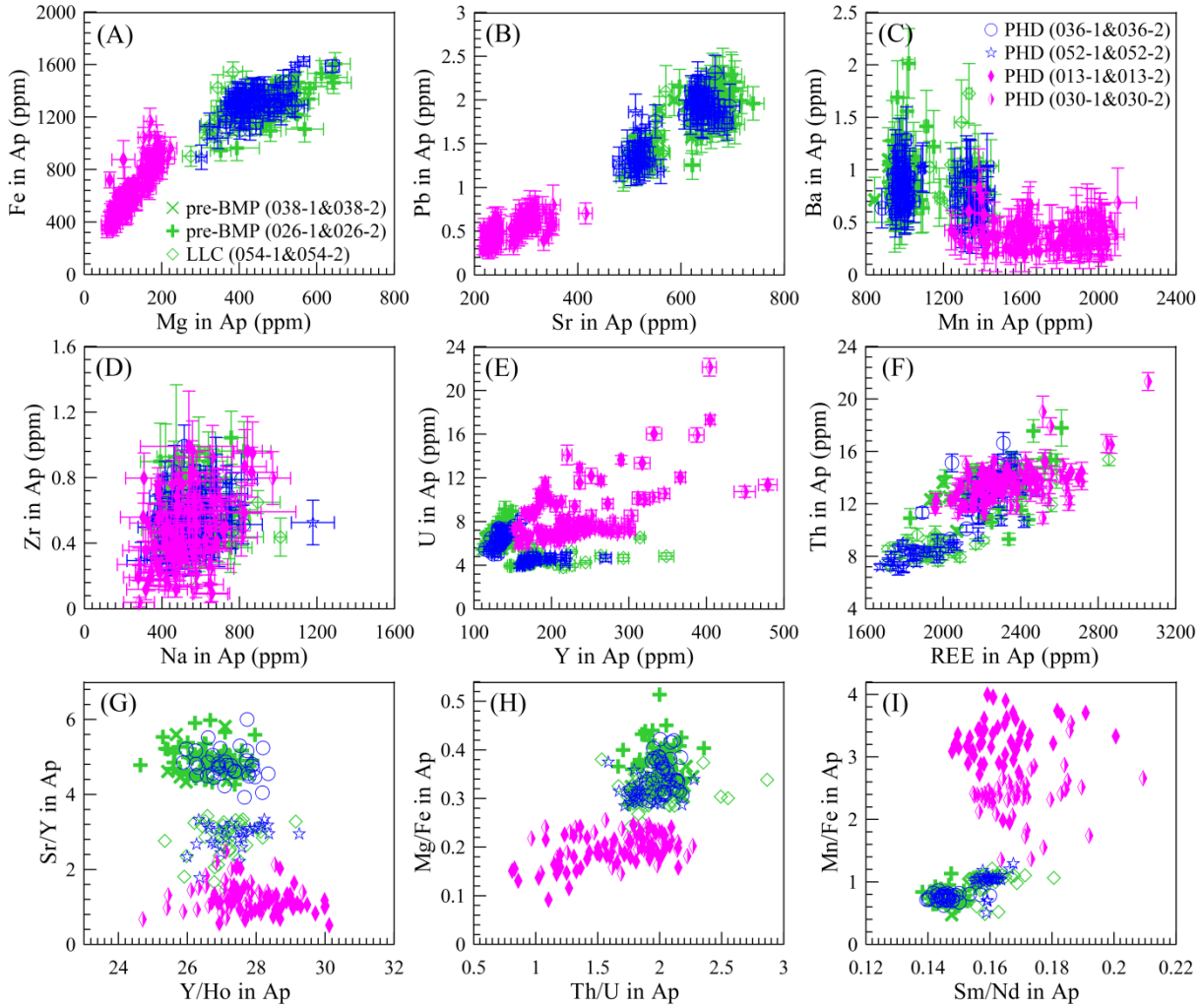

Fig. 5. Plots of (A) Fe versus Mg, (B) Pb versus Sr, (C) Ba versus Mn, (D) Zr versus Na, (E) U versus Y, (F) Th versus REE, (G) Y/Ho versus Sr/Y, (H) Th/U versus Mg/Fe and (I) Sm/Nd versus Mn/Fe for apatite from fresh and altered rocks at the Black Mountain porphyry Cu deposit.

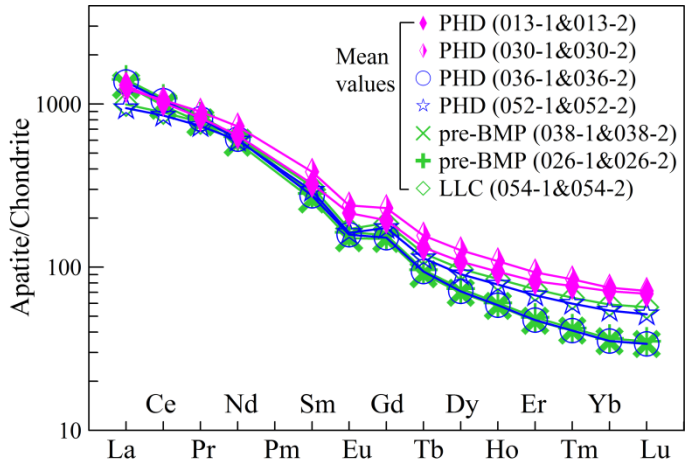

Fig. 6. Chondrite-normalized mean REE patterns of apatite from fresh and altered rocks at the Black Mountain porphyry Cu deposit. Chondrite REE values from Taylor and McLennan (1985).

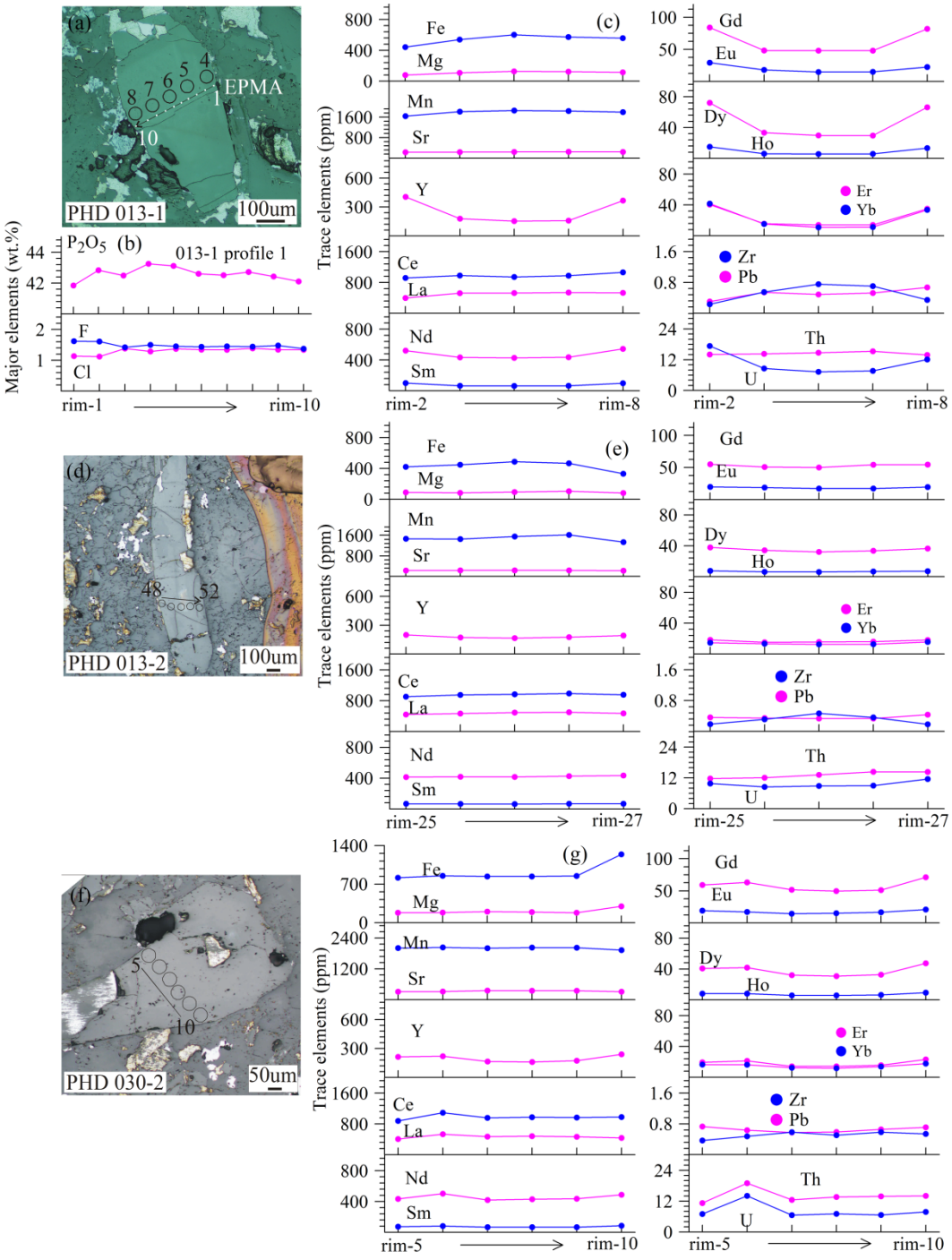

Fig. 7-1. Reflected-light photomicrographs of representative apatite grains from fresh and altered rocks, with measured EPMA and LA-ICP-MS transects showing the variations of P_2O_5, F, Cl (wt.%), Fe, Mg, Mn, Sr, Y, La, Ce, Nd, Sm, Gd, Eu, Dy, Ho,

Er, Yb, Zr, Pb, Th, U (ppm). Lines and arrows on photomicrographs show the location and direction of EPMA transects and circles correspond to the LA-ICP-MS spot position.

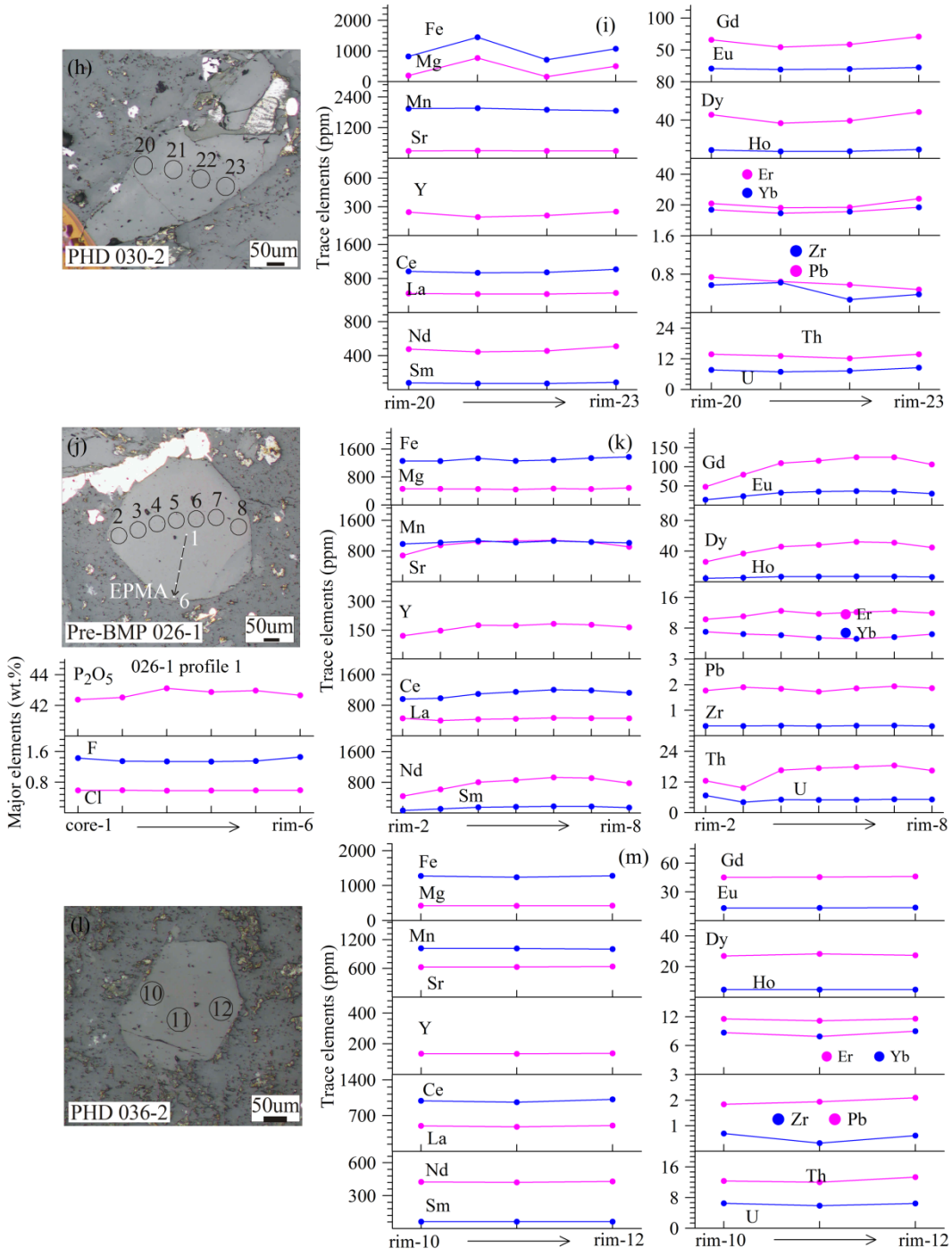

Fig. 7-2 continued.

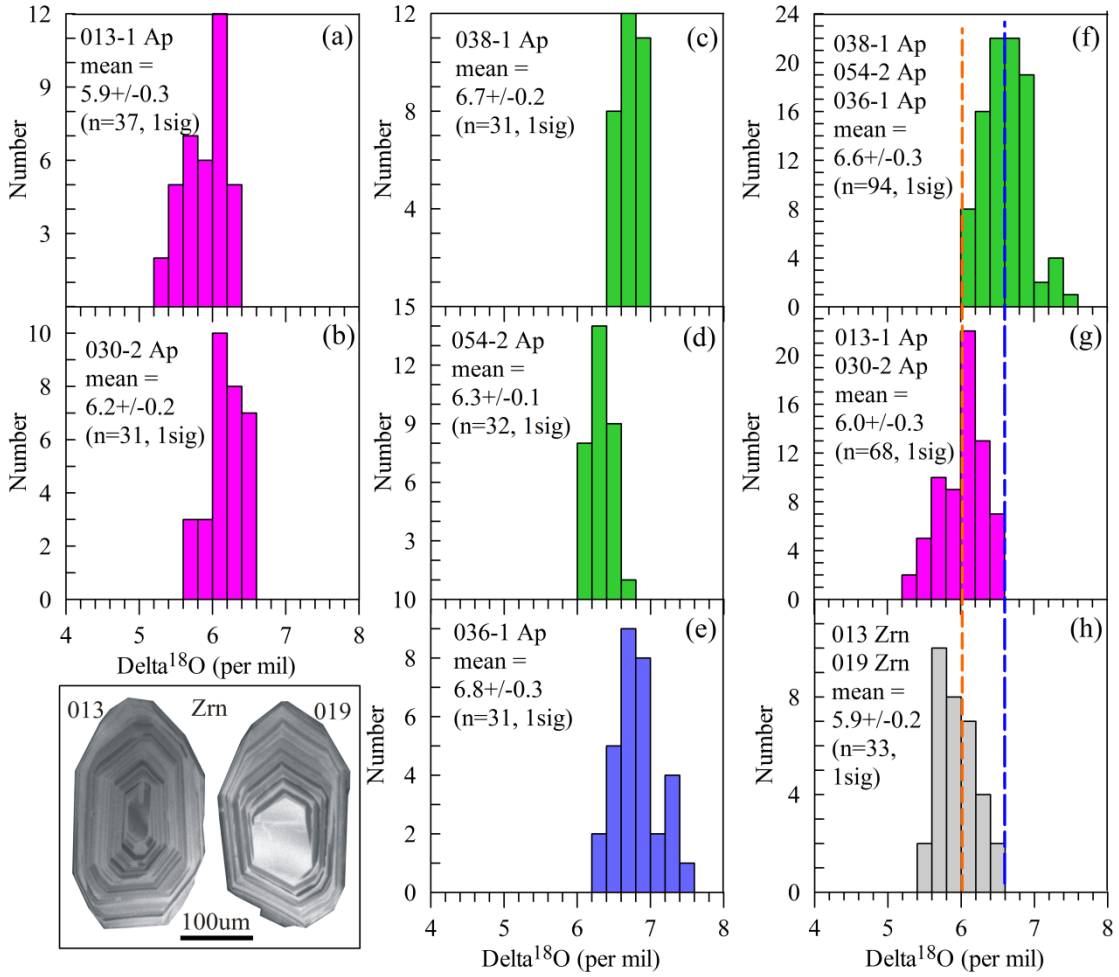

Fig. 8. Histograms of SIMS $\delta^{18}O$ (‰) showing the variation of apatite $\delta^{18}O$ in fresh rocks (013-1, 030-2), altered rocks (038-1, 054-2, 036-1) and zircon from the syn-mineralized diorite porphyry (013, 019). The insert figures are representative CL images of zircon from samples 013 and 019.

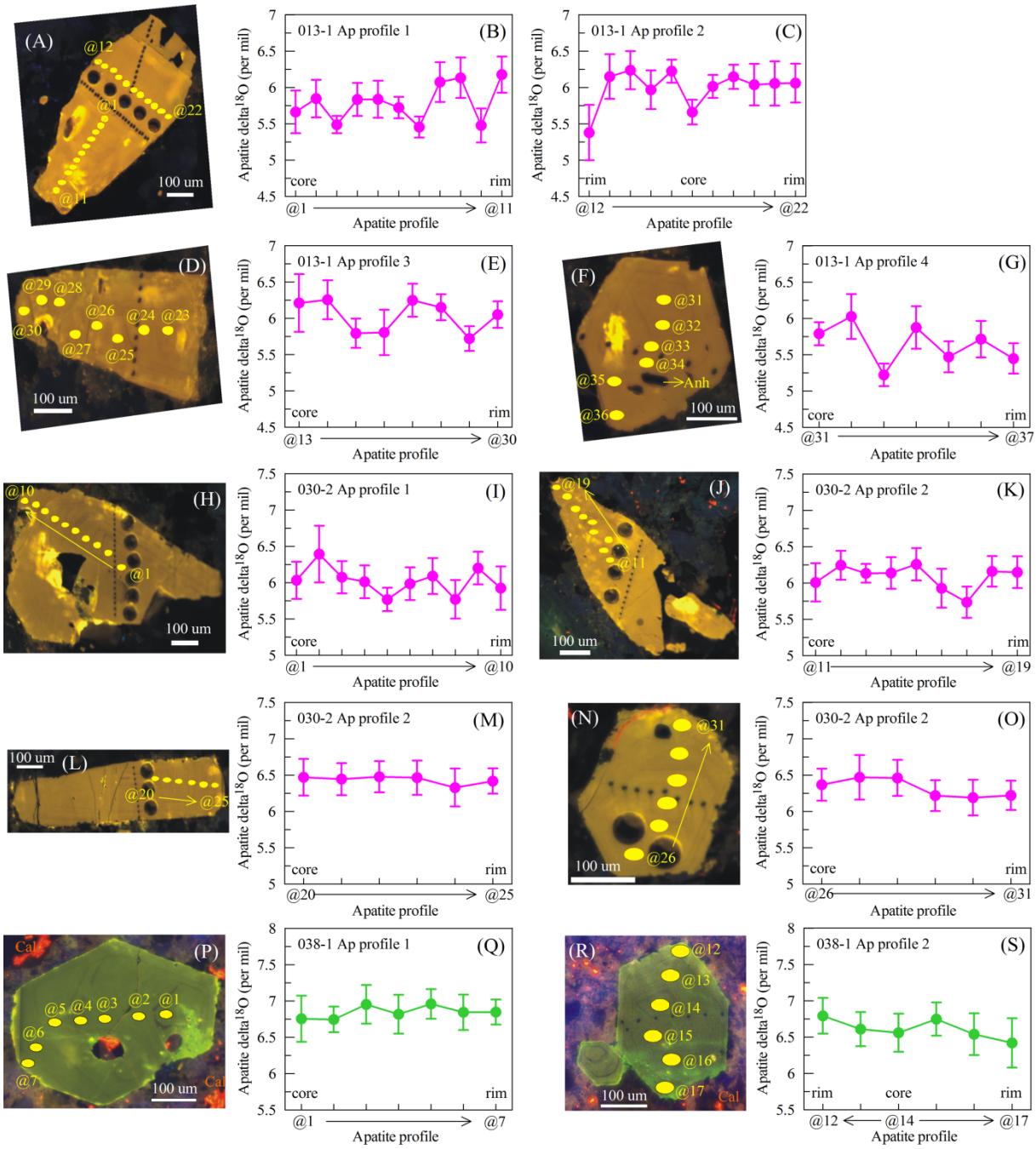

Fig. 9. CL images of representative apatite grains in fresh and altered rocks, and measured SIMS $\delta^{18}O$ transects (yellow filled cricles) showing the variations of $\delta^{18}O$ (‰). The big black holes on CL images (A, H, J, L, N) show the location of LA-ICP-MS spots.

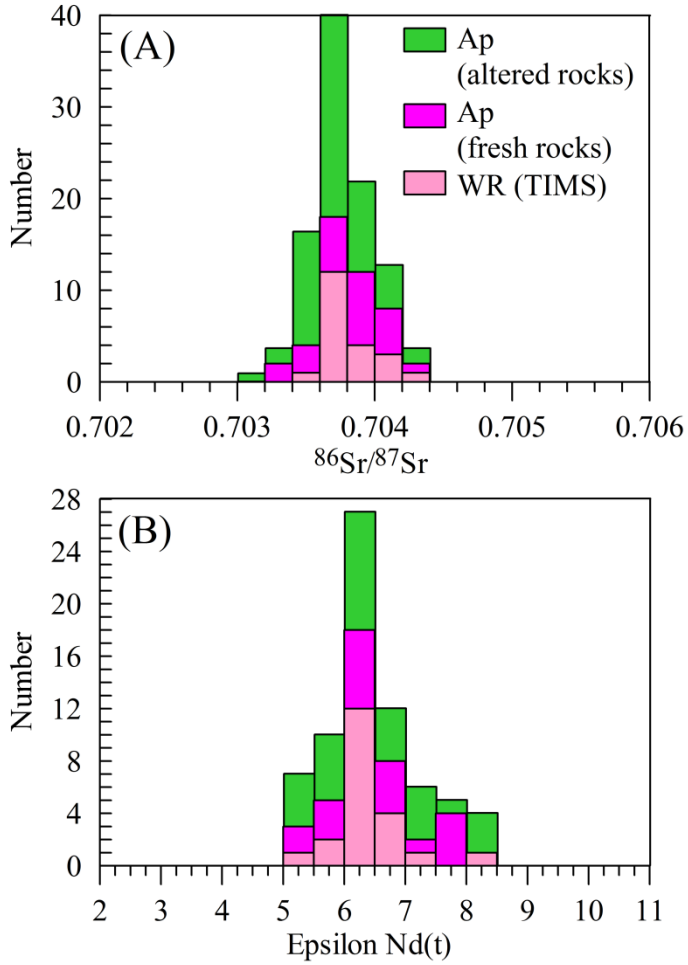

Fig. 10. Histograms of $^{86}Sr/^{87}Sr$ (A) and εNd(t) (B) showing the Sr-Nd isotopic variations of apatite in fresh and altered rocks, and whole rock (WR) from these rocks. WR Sr-Nd isotopes were obtained by thermal ionization mass spectrometry (TIMS) from Hollings et al. (2011, 2013).

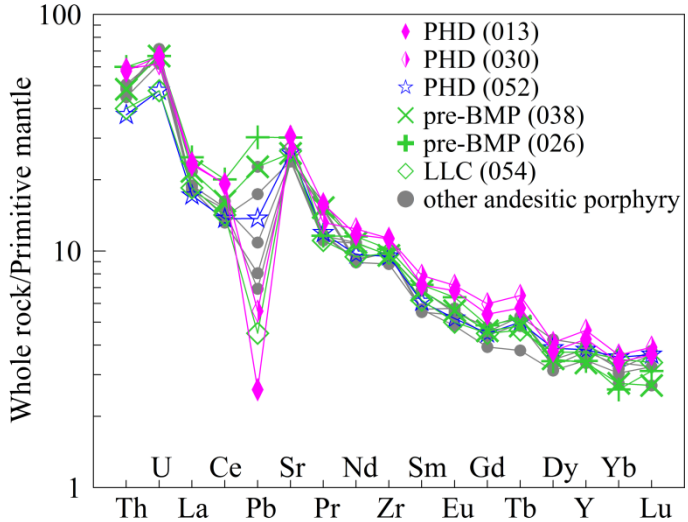

Fig. 11. Primitive mantle-normalized plots for intrusive samples from Black Mountain.

1179 The whole-rock geochemical data are from Hollings et al. (2013). The primitive mantle
1180 normalizing values are from Sun and McDonough (1989).
1181

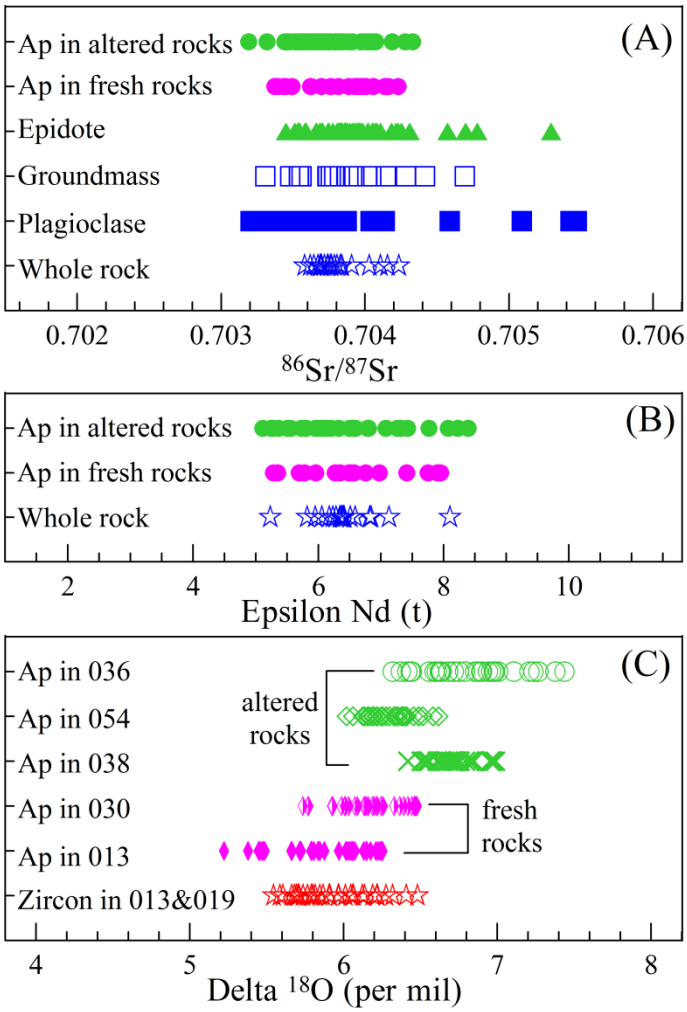

1182

1183 Fig. 12. Plots of (A) $^{86}Sr/^{87}Sr$, (B) εNd(t) and (C) $\delta^{18}O$ for apatite from fresh and altered
1184 rocks with data for whole rock (TIMS; Hollings et al., 2013), plagioclase phenocrysts,
1185 groundmass and hydrothermal epidote (all LA-MC-ICP-MS; Cao et al., 2020), and
1186 zircon $\delta^{18}O$ plotted for comparison.
1187

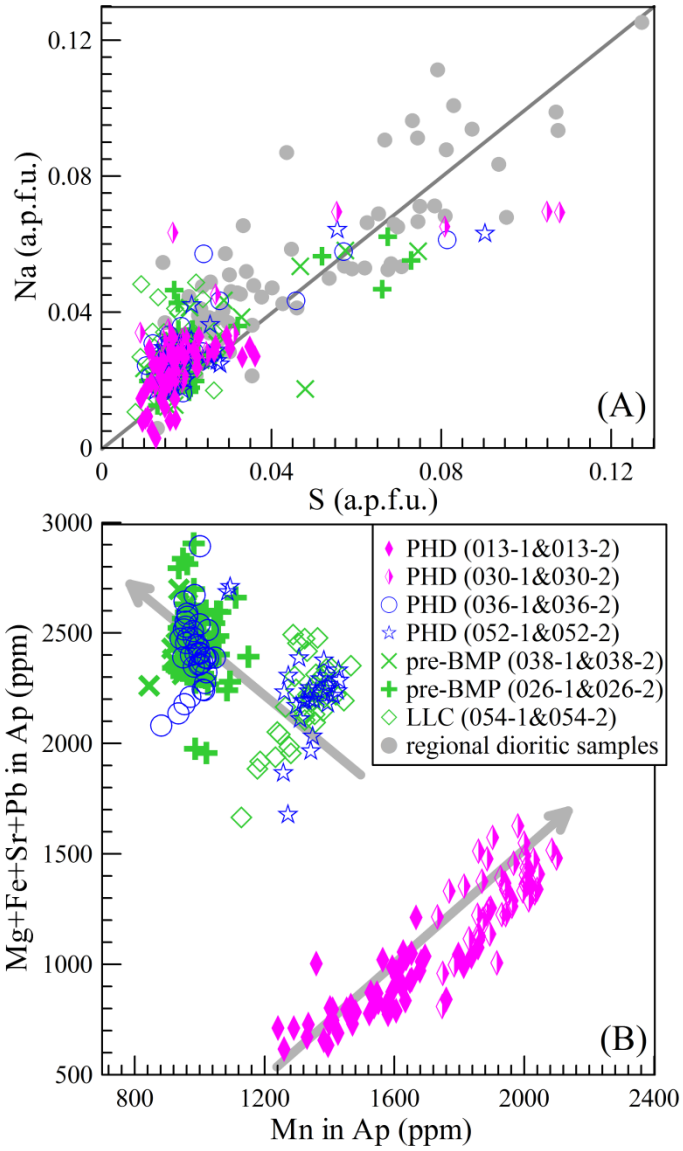

1188

1189 Fig. 13. Plots of (A) S versus Na (a.p.f.u.) and (B) Mn versus Mg+Fe+Sr+Pb for apatite
1190 from fresh and altered rocks at the Black Mountain porphyry Cu deposit. The data for
1191 regional samples are from Cao et al. (2018b).

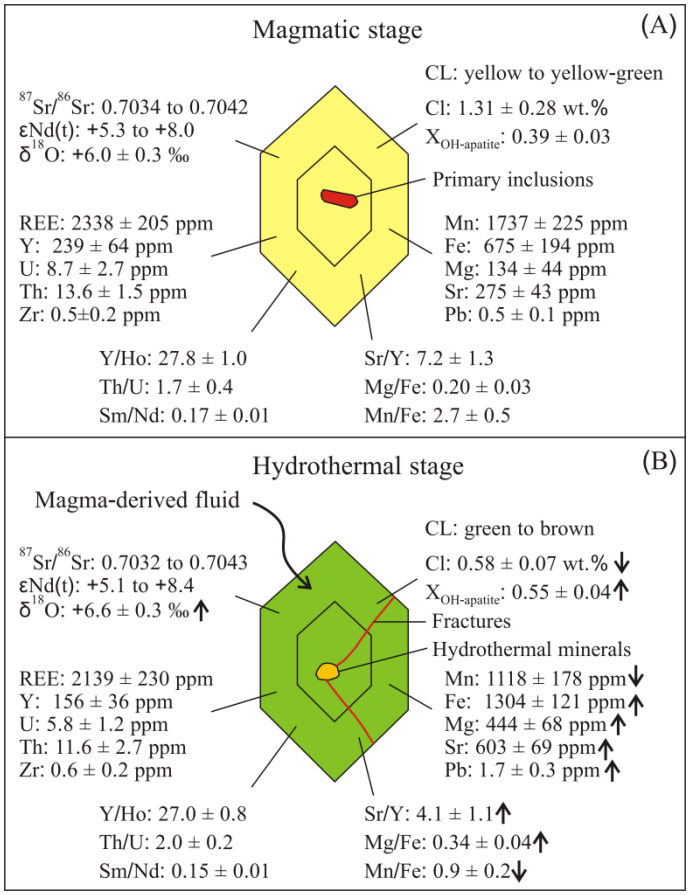

Fig. 14. Schematic figure illustrating the formation of magmatic and replacement apatite in the Black Mountain porphyry Cu deposit. (A) Magmatic apatite formed during the magmatic stage. (B) The magmatic apatite was replaced by hydrothermal fluids with decreases in Cl and Mn, increases in Fe, Mg, Sr, Pb, and retention of REE, Y, Th, U, Zr and Nd isotope compositions. The similar Sr isotope ratios between magmatic and replaced apatite indicate the same deep magma chamber source for both the magma and fluids. The slightly higher $\delta^{18}O$ values suggest fluid boiling in preliminary high temperatue single-phase supercritical fluids.

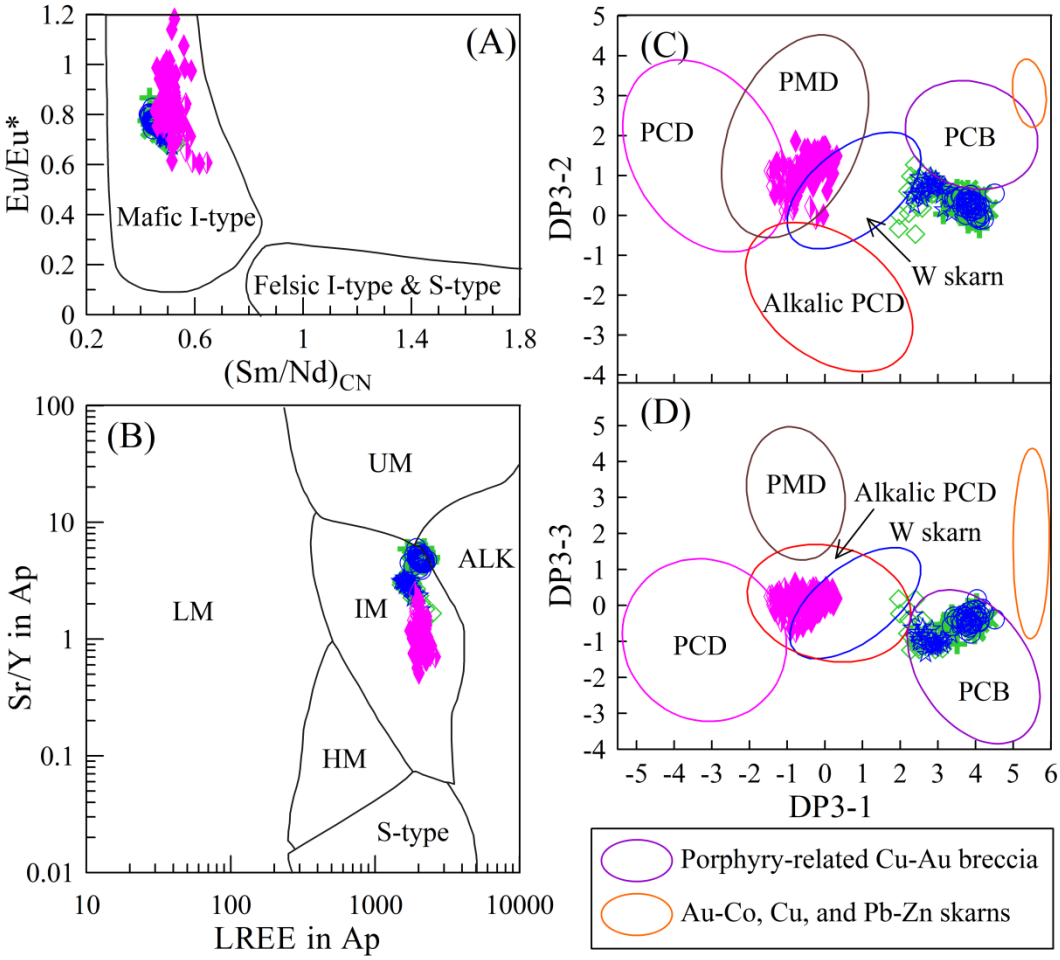

Fig. 15. Plots of (A) $(Sm/Nd)_{CN}$ versus Eu/Eu* (afer Sha and Chappell, 1999), (B) LREE (La-Nd) versus Sr/Y (after O'Sullivan et al., 2020), DP3-1 versus (C) DP3-2 and (D) DP3-3 (after Mao et al., 2016). Abbreviations: ALK = alkali-rich igneous rocks; IM = mafic I-type granitoids and mafic igneous rocks; LM = low- and medium-grade metamorphic and metasomatic; HM = partial-melts, leucosomes or high-grade metamorphic; S = S-type granitoids and high aluminium saturation index felsic I-types; UM = ultramafic rocks including carbonatites, lherzolites and pyroxenites; PCD = porphyry Cu ± Mo ± Au deposits; PMD = porphyry Mo deposits; PCB = porphyry-related Cu-Au breccia.

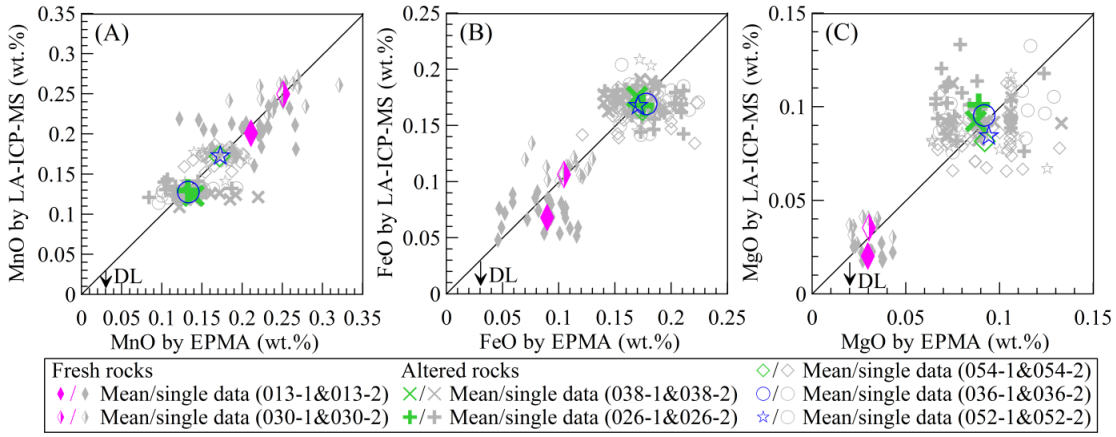

Fig. A.1. Plots of the average and single results for (A) MnO, (B) FeO and (C) MgO analyzed seperately by EPMA and LA-ICP-MS showing good consistency for different methods. DL = detection limit.

Table 1
Summary of mean values of analyzed apatite samples in fresh and altered rocks from the Black Mountain porphyry Cu deposit.

Type	Apatite in fresh syn-mineralized dioritic porphyry				Apatite in altered pre-mineralized dioritic porphyry						Apatite in altered syn-mineralized dioritic porphyry			
Sample	013 Ap		030 Ap		038 Ap		026 Ap		054 Ap		036 Ap		052 Ap	
	Mean	1σ	Mean	1σ	Mean	1σ	Mean	1σ	Mean	1σ	Mean	1σ	Mean	1σ
EPMA, wt.%														
P_2O_5	41.68	0.40	42.11	0.60	42.02	0.37	42.57	0.48	42.52	0.47	42.77	0.67	42.05	0.45
CaO	53.30	0.65	54.04	0.83	54.35	0.60	54.68	0.60	54.31	0.51	54.71	0.54	54.18	0.53
SiO_2	0.15	0.11	0.22	0.20	0.16	0.11	0.21	0.17	0.33	0.22	0.14	0.14	0.24	0.17
Al_2O_3	0.05	0.10	0.13	0.28	0.04	0.09	0.08	0.16	0.10	0.12	0.11	0.24	0.07	0.08
FeO	0.09	0.02	0.10	0.02	0.17	0.02	0.17	0.02	0.17	0.02	0.18	0.02	0.17	0.01
MnO	0.21	0.04	0.25	0.02	0.14	0.03	0.13	0.02	0.17	0.02	0.13	0.02	0.17	0.02
MgO	0.03	0.03	0.03	0.03	0.09	0.02	0.09	0.02	0.09	0.02	0.09	0.02	0.09	0.02
Na_2O	0.06	0.03	0.10	0.05	0.09	0.04	0.09	0.04	0.09	0.03	0.09	0.04	0.09	0.04
Cl	1.07	0.21	1.54	0.14	0.58	0.06	0.57	0.09	0.60	0.06	0.59	0.06	0.54	0.06
F	1.65	0.19	1.49	0.13	1.32	0.18	1.40	0.12	1.46	0.15	1.36	0.13	1.43	0.16
SO_3	0.14	0.06	0.21	0.19	0.19	0.11	0.19	0.12	0.14	0.04	0.18	0.12	0.19	0.13
LA-ICP-MS, ppm														
Na	500.9	150.5	550.4	137.8	519.2	54.7	535.8	111.0	534.7	144.4	584.8	115.1	531.3	162.6
Mg	97.8	22.3	171.1	25.1	179.3	35.2	300.0	64.7	396.1	56.8	460.8	52.2	407.4	56.3
Mn	1552	145	1929	89	1598	37	1374	47	1206	72	983	32	1330	85
Fe	528.7	110.0	827.0	136.2	769.5	58.6	987.4	127.9	1195.3	124.4	1314.7	103.9	1301.9	139.5
Ga	3.90	0.70	4.00	0.74	3.91	0.66	3.96	0.90	4.01	0.95	4.10	0.51	3.49	0.45
Sr	244.8	31.6	307.4	26.0	325.1	28.7	471.6	109.2	569.2	21.4	642.5	25.4	516.5	16.8
Y	225.8	64.7	251.9	60.9	219.2	7.6	187.4	13.8	169.8	43.4	135.0	8.6	181.8	24.7
Zr	0.48	0.24	0.46	0.22	0.49	0.12	0.52	0.18	0.55	0.15	0.59	0.13	0.46	0.16
Ba	0.40	0.14	0.39	0.12	0.46	0.13	0.63	0.28	0.80	0.23	0.84	0.17	0.75	0.21
La	478.3	49.9	453.5	32.8	461.3	28.9	473.0	45.9	446.5	34.2	501.3	33.1	346.1	26.3
Ce	976.9	72.3	1012.1	75.1	973.3	50.6	990.1	77.0	952.1	94.8	1004.1	58.3	813.5	69.8

Pr	112.6	9.0	123.0	13.1	114.3	5.3	115.8	17.5	112.9	13.4	111.4	5.3	100.6	9.8
Nd	456.2	42.7	518.2	70.7	469.6	20.0	473.1	121.0	463.7	62.6	433.2	20.9	425.1	45.4
Sm	74.8	10.9	88.7	17.5	77.5	2.7	76.0	27.8	73.2	12.5	63.3	3.9	68.0	7.9
Eu	18.7	3.6	20.8	2.8	18.3	0.6	17.4	5.8	16.0	2.5	13.7	0.8	14.1	1.4
Gd	59.3	10.7	70.4	15.7	61.2	2.7	58.4	20.0	55.9	11.3	46.4	2.8	53.3	6.8
Tb	7.6	1.7	9.0	2.3	7.8	0.3	7.1	1.9	6.7	1.5	5.4	0.4	6.6	0.9
Dy	41.2	10.9	48.3	12.7	41.4	1.4	36.9	6.1	34.1	8.3	27.1	1.8	34.5	5.0
Ho	8.0	2.2	9.2	2.4	7.9	0.3	6.9	0.6	6.3	1.7	5.0	0.3	6.7	1.0
Er	20.4	6.2	23.1	6.2	19.9	0.7	16.9	0.8	15.4	4.5	11.8	0.8	16.7	2.7
Tm	2.7	0.9	3.0	0.8	2.6	0.1	2.1	0.2	1.9	0.6	1.5	0.1	2.1	0.3
Yb	17.7	6.1	18.6	4.2	16.3	0.7	13.2	1.2	11.9	3.4	8.7	0.6	13.4	2.1
Lu	2.6	0.9	2.7	0.6	2.4	0.1	1.9	0.2	1.7	0.5	1.3	0.1	2.0	0.3
Pb	0.5	0.1	0.6	0.1	0.7	0.1	1.2	0.2	1.5	0.2	1.9	0.1	1.4	0.2
Th	13.4	1.0	13.7	1.9	13.3	1.2	13.4	1.9	12.1	1.7	13.1	1.6	8.3	0.9
U	9.1	2.5	8.2	2.7	8.1	0.5	7.5	1.0	6.1	0.5	6.5	0.7	4.4	0.3
ΣREE	2277	176	2401	216	2273	109	2288	253	2197	247	2234	116	1903	177
Eu*	0.86	0.13	0.82	0.08	0.81	0.02	0.79	0.02	0.75	0.02	0.78	0.02	0.72	0.02
Y/Ho	28.2	0.9	27.3	0.9	27.2	0.7	26.7	0.7	26.3	0.7	27.2	0.7	27.4	0.8
Th/U	1.56	0.37	1.75	0.31	1.71	0.14	1.85	0.42	1.96	0.25	2.03	0.09	1.88	0.16
Sm/Nd	0.16	0.01	0.17	0.01	0.16	0.00	0.16	0.01	0.15	0.01	0.15	0.00	0.16	0.00
Mg/Fe	0.19	0.03	0.21	0.03	0.22	0.02	0.28	0.04	0.32	0.03	0.35	0.03	0.31	0.02
Sr/Y	1.16	0.35	1.30	0.38	1.75	0.40	3.02	0.49	3.69	0.49	4.78	0.39	2.89	0.36
Mn/Fe	3.02	0.45	2.39	0.39	2.38	0.03	1.70	0.10	1.10	0.08	0.75	0.06	1.04	0.14
SIMS, ‰														
$\delta^{18}O$	5.88	0.29	6.16	0.23	6.72	0.16			6.32	0.15	6.81	0.30		
LA-MC-ICP-MS														
$^{87}Sr/^{86}Sr$	0.70387	0.00015	0.70379	0.00029	0.70374	0.00020	0.70369	0.00015	0.70388	0.00029	0.70367	0.00026	0.70368	0.00016
$^{147}Sm/^{144}Nd$	0.1041	0.0071	0.1064	0.0042			0.0896	0.0027	0.0991	0.0024	0.0910	0.0023	0.1054	0.0114
$(^{143}Nd/^{144}Nd)_i$	0.51299	0.00004	0.51295	0.00003			0.51298	0.00006	0.51298	0.00005	0.51294	0.00004	0.51296	0.00003
εNd(t)	7.0	0.7	6.1	0.7			6.8	1.1	6.7	0.9	5.9	0.7	6.4	0.5